# PROBING BEYOND STANDARD MODEL WITH COHERENT ELASTIC SCATTERING OF NEUTRINOS

A Dissertation

by

SHU LIAO

Submitted to the Office of Graduate and Professional Studies of
Texas A&M University
in partial fulfillment of the requirements for the degree of

DOCTOR OF PHILOSOPHY

| | |
|---|---|
| Chair of Committee, | Bhaskar Dutta |
| Committee Members, | Stephen A. Fulling |
| | Teruki Kamon |
| | Louis Strigari |
| Head of Department, | Grigory Rogachev |

May 2020

Major Subject: Physics

ABSTRACT

This work is to probe the potential of constraining various parameters of physics beyond Standard Model (BSM) using the coherent scattering of neutrinos from reactors, accelerators, and sun. In this work, a discovery potential of ultra-low energy threshold detector and a possibility of probing non-standard neutrino interaction in future direct dark matter detection experiments are presented. We also show the complementarity between different types of coherent neutrino scattering experiments, the current constraints and future sensitivity of coherent elastic neutrino-nucleus scattering in kinetic mixing $q^2$ form factor scenarios. We also analyze the COHERENT data release with energy and timing information using likelihood analysis in Bayesian framework. We find that neutrino scattering experiments gives notable results in the scenarios listed. And we also find dark matter signals might be hidden inside the released data.

# DEDICATION

To my parents, who give all their love to me.

ACKNOWLEDGMENTS

We acknowledge the Texas A&M University Brazos HPC cluster that contributed to the research presented here.

The contents of this work first appeared in the following articles and have been reproduced with permission:

J. B. Dent, B. Dutta, S. Liao, J. L. Newstead, L. E. Strigari, and J. W. Walker, "Probing light mediators at ultralow threshold energies with coherent elastic neutrino-nucleus scattering," *Phys. Rev.* **D96** no. 9, (2017) 095007, arXiv:1612.06350 [hep-ph].


J. B. Dent, B. Dutta, S. Liao, J. L. Newstead, L. E. Strigari, and J. W. Walker, "Accelerator and reator complementarity in coherent neutrino-nucleus scattering," *Phys. Rev.* **D97** no. 3, (2018) 035009, arXiv:1711.03521 [hep-ph]. 

M. Abdullah, J. B. Dent, B. Dutta, G. L. Kane, S. Liao, and L. E. Strigari, "Coherent elastic neutrino nucleus scattering as a probe of a Z through kinetic and mass mixing effects," *Phys. Rev.* **D98** no. 1, (2018) 015005, arXiv: 1803.01224 [hep-ph]. 

A. Datta, B. Dutta, S. Liao, D. Marfatia, and L. E. Strigari, "Neutrino scattering and B anomalies from hidden sector portals," *JHEP* **01**(2019) 091, arXiv: 1808.02611 [hep-ph]. 

B. Dutta, S. Liao, L. E. Strigari, and J. W. Walker, "Non-standard interactions of solar neutrinos in dark matter experiments," *Phys. Lett.* **B773** (2017) 242-246, arXiv:

1705.00661 [hep-ph]. Published by the Elsevier under the terms of the Creative Commons Attribution 4.0 International license

B. Dutta, S. Liao, S. Sinha, and L. E. Strigari, "Searching for Beyond the Standard Model Physics with COHERENT Energy and Timing Data," *Phys. Rev. Lett.* **123** no. 6, (2019) 061801, arXiv: 1903.10666 [hep-ph]. Published by the American Physical Society under the terms of the Creative Commons Attribution 4.0 International license

B. Dutta, D. Kim, S. Liao, J.-C. Park, S. Shin, and L. E. Strigari, "Dark matter signals from timing spectra at neutrino experiments," arXiv: 1906.10745 [hep-ph]. Submitted to Physical Review Letters

# CONTRIBUTORS AND FUNDING SOURCES

*Contributors*

This work was supported by a dissertation committee consisting of Professors Bhaskar Dutta [advisor], Louis Strigari, and Teruki Kamon of the Department of Physics and Astronomy and Professor Stephen Fulling of the Department of Mathematics.

Work for the dissertation was conducted by the student in collaboration with Professors Bhaskar Dutta and Louis Strigari of the Department of Physics and Astronomy, Professors James Dent and Joel Walker of Sam Houston State University, Jayden Newstead of Purdue University, Mohamed Abdullah of Texas A&M University, Professor Gordon Kane of Michigan University, Professor Danny Marfatia of Hawaii University, Professor Samiran Sinha of Texas A&M University, Doojin Kim of Texas A&M University, Professor Jong-Chul Park of Chungnam National University, Professor Seodong Shin of Chicago University.

*Funding Sources*

Graduate study was supported by COS-STRP (TAMU), MI, and DOE Grant desc0010813.

TABLE OF CONTENTS

Page

Page

LIST OF FIGURES

FIGURE Page

FIGURE Page

# LIST OF TABLES

TABLE Page

# 1. INTRODUCTION

The Standard Model (SM) of particle physics expects a neutral current interaction between neutrino and quarks/leptons mediated by a gauge boson $Z$. Rich pheromones of this interaction provide not only a better understanding of SM but also beyond Standard Model (BSM) such as non-standard interactions (NSI) of neutrinos, neutrino oscillations. In addition to understanding neutrino interactions, experiments measuring neutral current interactions of neutrinos can also be a powerful probe of new particles such as dark matter (DM) [1] particles and axion-like particles (ALP) [2].

The neutral current interaction can be detected as the elastic scattering of neutrinos from a nucleus or an electron. At low recoil energy when the wave length of momentum transfer is comparable to nucleus size, the neutrino scattering from nucleus is enhanced by coherent effect [3]. Many experiments were built to measure such coherent elastic neutrino-nucleus scattering (CE$\nu$NS) events. For example, COHERENT experiment [4] uses stopped pions created by proton hitting on target to produce neutrino source, and detects CE$\nu$NS events with a CsI detector. The COHERENT group detected CE$\nu$NS signals for the first time in 2017 [5]. In addition to using an accelerator neutrino source, reactor neutrino source such as in MINER project has also been developed to measure CE$\nu$NS using a megawatt (MW) reactor as neutrino source at Texas A&M University [6]. Both of these experiments use ultra-low threshold detectors. In this work, we show that such experiments provide a powerful tool of probing light and heavy mediators of NSI of neutrinos in terms of vector, axial-vector, scalar and pseudo-scalar couplings [7]. We show that results from different types of detectors used in CE$\nu$NS experiments complements with each other and give better constraints on NSI parameter spaces [8].

The CE$\nu$NS experiments may also help to understand the explanations of B anomalies where there is a strong evidence of deviation from SM in the angular distribution

of $B \to K^* \mu^+ \mu^-$. We show that CE$\nu$NS experiments can examine the two possible explanation including kinetic mixing with extra $U(1)$ gauge [9] and $q^2$ form factor [10].

Neutrino interactions also play important roles in dark matter direct-detection experiments. These experiments designed for spin-independent WIMP-nucleus scatter cross-section will be challenged by the neutrino background from the Sun, supernovae, and atmosphere [11]. Thus, it is essential to understand what is the impact on the neutrino floor from non-standard interactions. With multi-ton dark matter direct-detection experiments such as XENONnT [12] will not only search for the signals from dark matter, but also serves as ideal detector for the neutrinos from the sun. In this work, we show that NSI parameter space can be probed by dark matter direct-detection experiments by considering both propagation and detection of the solar neutrinos [13].

After the first report of the detection of CE$\nu$NS signals, COHERENT group released the measured experiment data [14]. The data include not only the energy spectrum but also timing spectrum. We find that the timing data provide statistical information on the neutrino flavor distributions that is not attainable from the nuclear recoil energies alone. And by including the timing data we show the data favors BSM interpretation of the data over SM at a significance $\leq 2\sigma$ level [15]. Further more, we find there is an excess of 26 events corresponding to $2.4\sigma$ resides in prompt region of the data after cutting out the neutrino events with an energy cut. This excess cannot be explained by NSI of neutrinos. In fact, we find such timing distribution can be easily explained by the dark matters decay from dark photons. We therefore propose a novel strategy to search for dark matter with timing spectra at CE$\nu$NS experiments [1].

In this work, we discuss above aspects of neutrino elastic scattering experiments in detail.

## 2. NON-STANDARD INTERACTIONS AND ITS PARAMETER SPACE*

Many extensions of the SM has additional massive particles from hidden sectors. For example, grand unified theories, models for baryogenesis, and dark sector models all include massive mediators from hidden sector. Experiments designed for CE$\nu$NS and neutrino-electron scattering can provide an important probe of such massive mediators from hidden sector.

The potential hidden interactions between neutrino and other fermions can be treated as NSI of neutrinos. Since the CE$\nu$NS process is well predicted in SM [3], any measured deviation from it can provide a test of NSI of neutrinos. Besides CE$\nu$NS experiments, low threshold neutrino-electron elastic scattering experiments are also important in identifying NSI of neutrinos. Specifically, CE$\nu$NS experiments will put limits on the interactions between neutrino and quarks, while neutrino-electron elastic scattering experiments will put limits on the interactions between neutrino and electrons.

In this chapter we first summarize the non-standard interaction in terms four types of massive mediator: vector, axial-vector, scalar, and pseudo-scalar; then discuss the discovery limits of these interactions from CE$\nu$NS experiments and neutrino-electron elastic scattering experiments; finally we point out there is a complementarity between accelerator and reactor CE$\nu$NS experiments.

*Parts of this section are reprinted with permission from:

J. B. Dent, B. Dutta, S. Liao, J. L. Newstead, L. E. Strigari, and J. W. Walker, "Probing light mediators at ultralow threshold energies with coherent elastic neutrino-nucleus scattering," *Phys. Rev.* **D96** no. 9, (2017) 095007, `arXiv:1612.06350 [hep-ph]`. 

J. B. Dent, B. Dutta, S. Liao, J. L. Newstead, L. E. Strigari, and J. W. Walker, "Accelerator and reator complementarity in coherent neutrino-nucleus scattering," *Phys. Rev.* **D97** no. 3, (2018) 035009, `arXiv:1711.03521 [hep-ph]`. 

## 2.1 Theory and formalism

### *2.1.1 Flavor-universal non-standard interactions*

To show the powerfulness of an ultralow threshold energy detector as neutrino scattering experiment, we consider four simple neutral current mediator that transforms as vector, axial-vector, scalar, and pseudo-scalar under Lorentz group. For simplicity, with light mediator we only consider flavor-universal non-standard interactions. The general Lagrangians are:

$$\mathcal{L}_V = Z'_\mu(g_{\nu,Z'}\bar{\nu}_L\gamma^\mu\nu_L + g_{\ell,Z'}\bar{\ell}\gamma^\mu\ell + g_{q,Z'}\bar{q}\gamma^\mu q) \tag{2.1}$$

$$\mathcal{L}_{AV} = \tilde{Z}'_\mu(g_{\nu,Z'}\bar{\nu}_L\gamma^\mu\nu_L - g_{\ell,\tilde{Z}'}\bar{\ell}\gamma^\mu\gamma^5\ell - g_{q,\tilde{Z}'}\bar{q}\gamma^\mu\gamma^5 q) \tag{2.2}$$

$$\mathcal{L}_S = \phi(g_{\nu,\phi}\bar{\nu}\nu + g_{\ell,\phi}\bar{\ell}\ell + g_{q,\phi}\bar{q}q) \tag{2.3}$$

$$\mathcal{L}_{PS} = \tilde{\phi}(g_{\nu,\phi}\bar{\nu}\nu - i(g_{\ell,\tilde{\phi}}\bar{\ell}\gamma^5\ell + g_{q,\tilde{\phi}}\bar{q}\gamma^5 q)) \tag{2.4}$$

The Standard Model interactions between neutrino and other fermions includes $W^\pm$ and $Z$ bosons as mediator. Because the energy scale at neutrino scattering experiments are orders of magnitude lower compare to $W^\pm$ and $Z$ bosons masses, the SM interaction can be written as a four fermion effective interaction:

$$\mathcal{L}_{\rm SM} = 2\sqrt{2}G_F(J^{+\mu}J^-_\mu + J^\mu_Z J_{Z\mu}) \tag{2.5}$$

The first term $J^{+\mu}J^-_\mu$ only applies to neutrino-electron interaction in elastic scattering experiments because it can be re-written into neutral current form via Fierz transformation.

With the above Lagrangians, we first write the differential cross section for a neutrino scattering off a target of mass $m$ under vector and axial vector interaction since

they interfere with SM:

$$\frac{\mathrm{d}\sigma}{\mathrm{d}E_R} = \frac{G_F^2 m}{2\pi}\big((g_v+g_a)^2 + (g_v-g_a)^2\left(1-\frac{E_R}{E_\nu}\right)^2 + (g_a^2-g_v^2)\frac{mE_R}{E_\nu^2}\big)\,. \tag{2.6}$$

where $g_v$ and $g_a$ includes contribution from both SM and BSM. The $Z$ boson exchange from SM contributes $T_3 - 2Q_{em}\sin^2\theta_W$ and $T_3$ to $g_v$ and $g_a$ respectively, where $T_3$ is the diagonal generator of $SU(2)_L$, $Q_{\mathrm{em}}$ is the electromagnetic charge, and $\theta_W$ is the weak mixing angle. In the case of neutrino-electron elastic scattering, there is an additional contribution $+1$ for $g_v$ and $g_a$ from $t$-channel exchange of $W^\pm$ boson. The corresponding $g_v$ and $g_a$ for neutrino-electron scattering are:

$$g_v^e = \frac{1}{2} + 2\sin^2\theta_w + g_{\nu,Z'}g_{\ell,Z'}/(2\sqrt{2}G_F(m_{Z'}^2+q^2)) \tag{2.7}$$

$$g_a^e = \frac{1}{2} + g_{\nu,\tilde{Z}'}g_{\ell,\tilde{Z}'}/(2\sqrt{2}G_F(m_{\tilde{Z}'}^2+q^2)) \tag{2.8}$$

where $q^2 = 2mE_R$ is the square of four-momentum transferred.

In the case of CE$\nu$NS, we need to first find the corresponding $g_v$ and $g_a$ for nucleons. Because the scattering is coherent, the couplings are the sum of the contribution from all quarks in the nucleons because the scattering is coherent. We define the effective coupling to proton or neutron as:

$$g_v^p = \frac{1}{2} - 2\sin^2\theta_w + 3g_{\nu,Z'}g_{q,Z'}/(2\sqrt{2}G_F(m_{Z'}^2+q^2)) \tag{2.9}$$

$$g_a^p = \frac{1}{2} + 3g_{\nu,\tilde{Z}'}g_{q,\tilde{Z}'}/(2\sqrt{2}G_F(m_{\tilde{Z}'}^2+q^2)) \tag{2.10}$$

$$g_v^n = -\frac{1}{2} + 3g_{\nu,Z'}g_{q,Z'}/(2\sqrt{2}G_F(m_{Z'}^2+q^2)) \tag{2.11}$$

$$g_a^n = -\frac{1}{2} + 3g_{\nu,\tilde{Z}'}g_{q,\tilde{Z}'}/(2\sqrt{2}G_F(m_{\tilde{Z}'}^2+q^2)) \tag{2.12}$$

Thus the vector and axial-vector charge of neutrino-nucleus interaction can be written

as

$$Q_v = g_v^p Z + g_v^n N \tag{2.13}$$

$$Q_a = g_a^p \langle S_p \rangle + g_a^n \langle S_n \rangle \tag{2.14}$$

Putting all together, we can write the differential cross section for neutrino-nucleus scattering as:

$$\frac{\mathrm{d}\sigma}{\mathrm{d}E_R} = \frac{G_F^2 m_N}{\pi} \left[ \left( 1 - \frac{m_N E_r}{2E_\nu^2} \right) Q_v^2 F^2(E_r) + \left( 1 + \frac{m_N E_r}{2E_\nu^2} \right) Q_a^2 \frac{4(J_N+1)}{3J_N} \right] . \tag{2.15}$$

where $F^2(E_r)$ is Helm form factor [16]. We do not include a spin form factor as they do not vary much over the region of interest [17].

The scalar and pseudo-scalar NSI does not interfere with SM. Therefore, the differential cross section is SM plus additional contribution from scalar or pseudo-scalar couplings. The corresponding differential cross sections are:

$$\frac{\mathrm{d}\sigma}{\mathrm{d}E_R} = \frac{1}{4\pi E_\nu^2} \frac{g_{\nu,\phi}^2 g_{f,\phi}^2}{(2mE_R + m_\phi^2)^2} E_R m^2 \tag{2.16}$$

for scalar interactions, and:

$$\frac{\mathrm{d}\sigma}{\mathrm{d}E_R} = \frac{1}{8\pi E_\nu^2} \frac{g_{\nu,\tilde{\phi}}^2 g_{f,\tilde{\phi}}^2}{(2mE_R + m_{\tilde{\phi}}^2)^2} E_R^2 m \tag{2.17}$$

for pseudo-scalar interactions.

In the case of neutrino-nucleus scattering, we first define the effective Lagrangian for nucleons:

$$\mathcal{L}_{eff} = \langle \mathcal{N} | \phi \sum_q g_{q,\phi} \bar{q} q | \mathcal{N} \rangle = \phi g_{q,\phi} \left( \sum_q f_q^{\mathcal{N}} \frac{m_{\mathcal{N}}}{m_q} \right) \bar{\mathcal{N}} \mathcal{N} \tag{2.18}$$

where $f_q^{\mathcal{N}}$ is the nucleon form factor for scalar couplings with values from [18, 19].

Since the scattering is coherent, we get the differential cross section:

$$\frac{\mathrm{d}\sigma}{\mathrm{d}E_R} = \frac{1}{4\pi E_\nu^2}\frac{Q_s^2}{(2mE_R + m_\phi^2)^2} E_R m_N^2 \tag{2.19}$$

where $Q_s = g_{\nu,\phi} g_{q,\phi} \left( \sum_{\mathcal{N},q} f_q^{\mathcal{N}} \frac{m_{\mathcal{N}}}{m_q} \right)$ is the effective coupling for neutrino-nucleus scattering. As for pseudo-scalar interactions, the neutrino-nucleus cross section is negligible, because the cross section is proportional to $E_R^2$.

To further simplify the expression, in this chapter, we define $Q_s = f_n A$, $Q'_v = b_n A$, and $Q'_a = a_0 \langle S \rangle$, with $Q'_v$ and $Q'_a$ equal to $Q_v$ and $Q_a$ minus SM contribution.

### *2.1.2 Flavor-dependent heavy vector mediators*

In the context of neutrino oscillation, the most commonly investigated form of NSI is in terms of effective vector couplings with heavy mediators. The neutrino oscillation experiments already has various constraints on the parameter spaces of this type of NSI [20–22]. However, there are limits on the probes of NSI with oscillation experiments. Because oscillation experiments 1) are only sensitive to differences in flavor diagonal NSI components via differentially accred phase; 2) are unable to distinguish between up and down quarks; 3) suffer from degeneracies with LMA-Dark solution where different parameter spaces give exactly same oscillation phenomenous. The CE$\nu$NS experiments are complement to the oscillation experiments, as will be shown later in this section.

With heavy vector mediator, the NSI can be parametrized as:

$$\mathcal{L}_{NSI} = -\sqrt{2} G_F \sum_{\alpha,\beta,f} \bar{\nu}_{\alpha L} \gamma^\mu \nu_\beta \epsilon^f_{\alpha\beta} \bar{f} \gamma_\mu f \tag{2.20}$$

where $\alpha$, $\beta = e, \mu, \tau$ indicate the neutrino flavor, $f$ the fermion type. The differential cross section is:

$$\frac{d\sigma}{dE_R} = \frac{G_F^2 Q_V^2}{2\pi} m_N \left( 1 - \left( \frac{m_N E_R}{E_\nu^2} \right) + \left( 1 - \frac{E_R}{E_\nu} \right)^2 \right) F(q^2) \tag{2.21}$$

The "charge" $Q_v$ now includes flavor-changing couplings:

$$\begin{aligned} Q_v^2 &= \left[Z(g_p^v + 2\epsilon_{\alpha\alpha}^u + \epsilon_{\alpha\alpha}^d) + N(g_n^v + \epsilon_{\alpha\alpha}^u + 2\epsilon_{\alpha\alpha}^d)\right]^2 \\ &+ \sum_{\alpha\neq\beta} \left[Z(2\epsilon_{\alpha\beta}^u + \epsilon_{\alpha\beta}^d) + N(\epsilon_{\alpha\beta}^u + 2\epsilon_{\alpha\beta}^d)\right]^2 \end{aligned} \tag{2.22}$$

The neutrino oscillation experiments measure diagonal term of the effective NSI parameters defined as:

$$\epsilon_{\alpha\beta} = \sum_{f=u,d,e} Y_f(x)\epsilon_{\alpha\beta}^f \tag{2.23}$$

where $Y_f(x)$ is the average of the $f/e$ density ratio of the matter in which neutrino propagate.

## 2.2 Statistics analysis framework

We employ two statistic method in this chapter: profile likelihood test statistic (frequentist's method) for identifying the discovery limit for the flavor universal NSI couplings; and multi-parameter Bayesian framework for the flavor-dependent heavy vector NSI couplings. The profile likelihood test statistic is widely used in the analysis of NSI parameters, however, it lacks the power of evaluating multiple parameters at once and capture the correlation between the parameters. As a result, when we analyze the flavor-dependent heavy mediator NSI, we switch to Bayesian framework.

### *2.2.1 Profile likelihood analysis*

In this statistic frame work, we define the profile likelihood test statistic:

$$t_\mu = -2\log\frac{\mathcal{L}(\mu,\hat{\theta})}{\mathcal{L}(\hat{\mu},\hat{\hat{\theta}})} \tag{2.24}$$

where $\mu$ is the signal strength, $\frac{\sigma}{\sigma_{\rm SM}}$, and $\theta$ represents the nuisance parameters. Hatted parameters, $\hat{\theta}$ and $\hat{\mu}$, denote the values which maximize the likelihood (note that the parameters ($\hat{\theta}$) which maximize the likelihood for a given $\mu$ may not be the same as the

| component | $\nu$ flux ($cm^{-2}s^{-1}$) |
|---|---|
| TAMU reactor (at 2m) | $3.75(1 \pm 0.02) \times 10^{11}$ |
| SNS (at 20m) | |
| $\nu_\mu$ (prompt) | $1.05(1 \pm 0.1) \times 10^7$ |
| $\nu_e$ (delayed) | $1.05(1 \pm 0.1) \times 10^7$ |
| $\bar{\nu}_\mu$ (delayed) | $1.05(1 \pm 0.1) \times 10^7$ |
| Solar | |
| pp | $5.98(1 \pm 0.006) \times 10^{10}$ |
| $^7$Be | $5.00(1 \pm 0.07) \times 10^9$ |
| $^8$B | $5.58(1 \pm 0.14) \times 10^6$ |
| pep | $1.44(1 \pm 0.012) \times 10^8$ |

Table 2.1: Neutrino flux sources and their respective uncertainties in the flux normalizations. Reprinted with permission from [8].

parameters ($\hat{\hat{\theta}}$) that maximize for $\hat{\mu}$). We will use a binned likelihood function given by:

$$\mathcal{L} = \prod_i \frac{\nu_i^{n_i} e^{-\nu_i}}{n_i!} \prod_j e^{-\frac{1}{2\delta_j^2}(1-N_j)^2} \tag{2.25}$$

Here $\nu_i$ and $n_i$ are the expected (SM) and observed events in each bin, and the second product is a Gaussian likelihood summed over the nuisance parameters, in this case is the background and flux component normalizations $N_j$. The numbers for flux normalizations are summarized in Table 2.1. The SNS flux and uncertainty was taken from [5]. The Solar components are derived from the high metallicity Solar model as outlined in Ref. [23]. We calculate the expected number of events $\nu_i$ under various low threshold detector setup summarized in Table 2.2.

In order to calculate the experiment limit based on the specifications shown above, we use a binned likelihood function, Equation. 2.25 with log-spaced bins. The likelihood is used to calculate the log-likelihood ratio and generate the test statistic $q_0$, from which we may estimate the expected median significance of an experiment via the Asimov dataset [24].

$$t_\mu = -2\log\frac{\mathcal{L}(\mu, \hat{\theta})}{\mathcal{L}(\hat{\mu}, \hat{\hat{\theta}})} \tag{2.26}$$

| Name | Target | Exposure (kg.days) | $E_{th}$ (eV) | background (dru) |
|---|---|---|---|---|
| Ge | germanium | 10,000 | 100 | 100±10 |
| Ge II | germanium | 10,000 | 10 | 10 ±1 |
| Ge II(low BG) | germanium | 10,000 | 10 | $(1\pm.1)\times10^{-4}$ |
| Si | silicon | 10,000 | 100 | 100±10 |
| Si II | silicon | 10,000 | 20 | 10 ±1 |
| CsI | Caesium-Iodide | 10,000 | 5,000 | $(1\pm.05)\times10^{-3}$ |

Table 2.2: Detector specifications for light mediator analysis. Reprinted with permission from [8].

The corresponding confidence level is then $Z = \sqrt{t_\mu}$, because we only have one degree of freedom in this analysis.

### *2.2.2 Multi-parameter Bayesian analysis*

We calculate the posterior probability distribution NSI parameter space $\theta$ giving data $D$ and prior information $I$ using Bayes' theorem:

$$\mathcal{P}(\theta|D,I) = \frac{\mathcal{L}(D|\theta,I)\pi(\theta|I)}{\epsilon(D|I)} \tag{2.27}$$

Here $\mathcal{L}(D|\theta,I)$ is the likelihood of a set of NSI parameters reproducing the observed (or simulated) data:

$$\mathcal{L}(D|\theta,I) = \prod_i \prod_j p(D_i|\lambda_i(\theta)) \tag{2.28}$$

with $j$ runs over energy bins, and $i$ runs over the detectors used in a given experimental configuration. The prior probability, $\pi(\theta|I)$, is taken to be uniform for the NSI parameters (i.e. there is no prior information), and taken to be Gaussian for the nuisance parameters. The priors are summarized in Table 2.3. Finally, the Bayesian evidence, $\epsilon(D|I)$, serves as a normalization factor.

We run this analysis under three different experiment configurations, summarized in Table 2.4, to show the complementarity of these experiments.

| Parameter | Prior range | Scale |
|---|---|---|
| $\epsilon^f_{\alpha\alpha}$ | (-1.5, 1.5) | linear |
| SNS flux | $(4.29 \pm 0.43) \times 10^9$ | Gaussian |
| Reactor flux | $(1.50 \pm 0.03) \times 10^{12}$ | Gaussian |
| SNS background | $(5 \pm 0.25) \times 10^{-3}$ | Gaussian |
| Reactor background | $(1 \pm 0.1)$ | Gaussian |

Table 2.3: Baseline priors used for the NSI parameters and nuisance parameters in this analysis. Fluxes are per $cm^2$·s, and backgrounds are per kg·day·keV. Reprinted with permission from [8].

| Name | Detector | Source | Exposure | Threshold |
|---|---|---|---|---|
| Current (COHERENT) | CsI | SNS (20m) | 4466 kg.days | 4.25 keV |
| Future (reactor) | Ge | 1GW reactor (20m) | $10^4$ kg.days | 100 eV |
| | Si | 1GW reactor (20m) | $10^4$ kg.days | 100 eV |
| Future (accelerator) | NaI | SNS (20m) | 1 tonne.year | 2 keV |
| | Ar | SNS (20m) | 1 tonne.year | 30 keV |

Table 2.4: Experimental configurations for experiment complementarity analysis. Reprinted with permission from [8].

### 2.3 Results and analysis

We show the discovery limits for Germanium and Silicon in Figure 2.1 and 2.2 correspondingly. The pseudo-scalar coupling for nucleus scattering is missing because, as stated in previous section, the neutrino-nucleus cross section is negligible. We first notice that all the limits plots share similar pattern in mediator mass versus coupling space. That is, for very light mediators, the discovery limits are independent of mediator mass; for very heavy mediators, the coupling sensitivity is dimensioned with a log-log slope of 2. This is because the contribution from BSM is always of the form $coupling/(m^2 + q^2)$. When $m \ll q$ (light mediator), BSM contribution is $coupling/q^2$ independent of mediator mass; when When $m \gg q$ (heavy mediator), BSM contribution is $coupling/m^2$, which indicates a constant slope line in log-log space ($\log(couplings) = 2\log(m)$). The "knee" of these plots centers around

$M_{Z'} \simeq \sqrt{2E_R m_X}$, marking the tuning point between light and heavy mediator.

The above analysis is done with flavor-universal NSI, and only one of the NSIs is turned on in the each of the analysis. We use this simplified approaches to demonstrate the ability of low-threshold detectors as probe of BSM. In the general case of flavor-dependent heavy mediator NSI under the context of neutrino oscillation experiments, we show that it is possible to break down the degeneracies of the NSI couplings by combining different CE$\nu$NS experiments.

We consider here four NSI parameters: $\epsilon^u_{ee}$, $\epsilon^u_{\mu\mu}$, $\epsilon^d_{ee}$, and $\epsilon^d_{\mu\mu}$, because reactor neutrino source only have electron neutrinos and accelerator neutrino source has electron and muon neutrinos. We show the results in Figure 2.3. As can be seen from the figure, the NSI parameter space breaks into individual "islands" with $ee$ component receiving more constraints than $\mu\mu$ components. This is because both accelerator and reactor neutrino source produce electron neutrino while only accelerator neutrino source produces muon neutrino. It results different sensitivity to each types of NSI parameters. If we can remove the background associated with the neutrino we will receive better sensitivity to the NSI parameters, as can be shown in Figure 2.4, the parameter space completely breaks down to four "islands" in the four dimension space. The other three "island" in the parameter space besides SM all degenerate with SM. That is, with the complementarity, we have removed as much as degeneracies as possible with combining reactor and accelerator based neutrino experiments, there will still few points in the parameter space that scattering experiments can not distinguish. To show the what constraints CE$\nu$NS experiments can put on the effective coupling in the neutrino oscillation experiments, we plot the result in Figure .2.5. As can be seen in the plot, the parameter space of effective is strongly constrained by the combination of accelerator and reactor neutrino experiments. Thus, the CE$\nu$NS experiments also provide great supplements to the oscillation experiments.

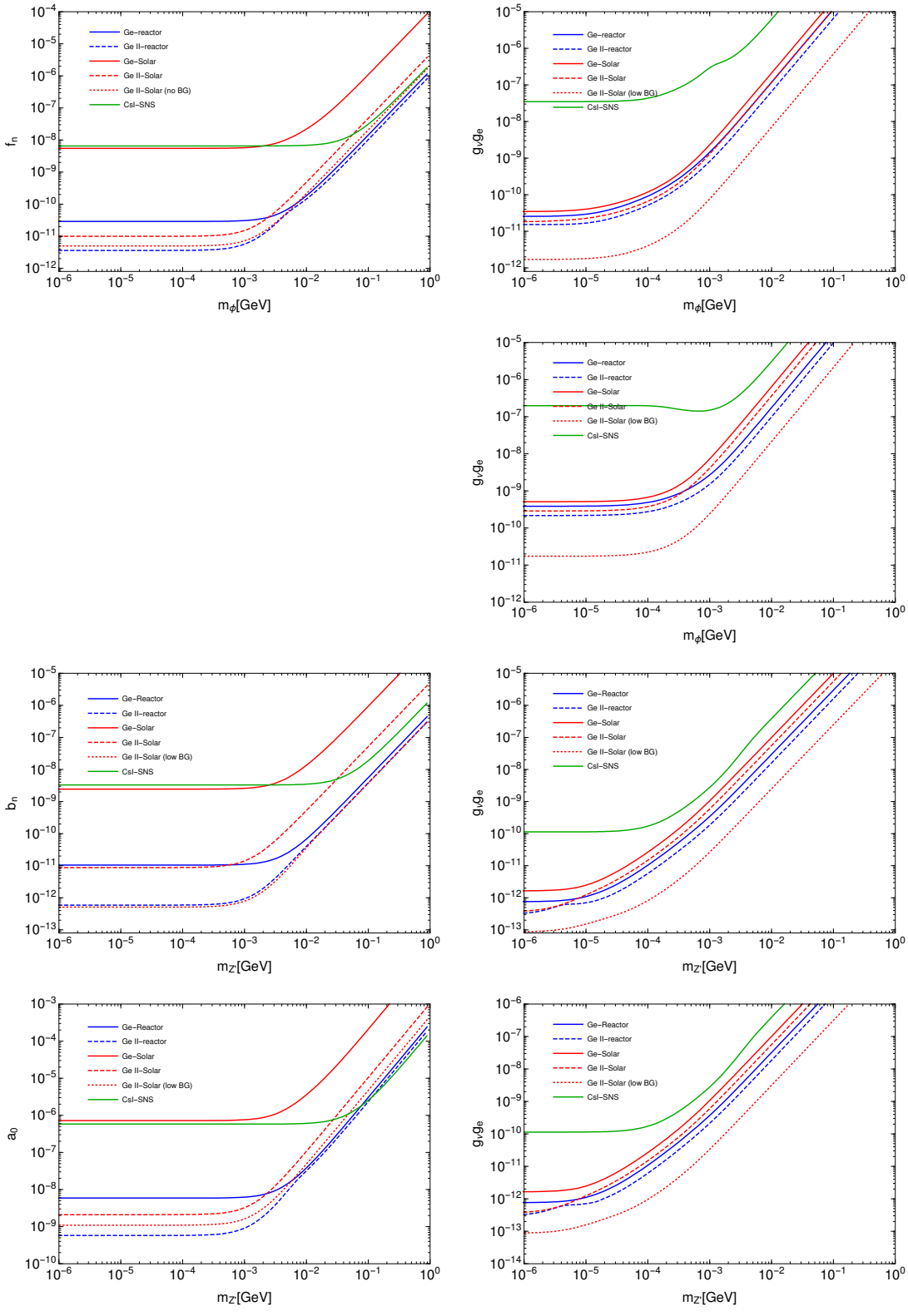


Figure 2.1: Discovery limits for neutrino scattering off germanium nuclei (left) and electrons (right), for the different BSM models (from top to bottom): scalar, pseudo-scalar, vector and axial-vector. Reprinted with permission from [7].

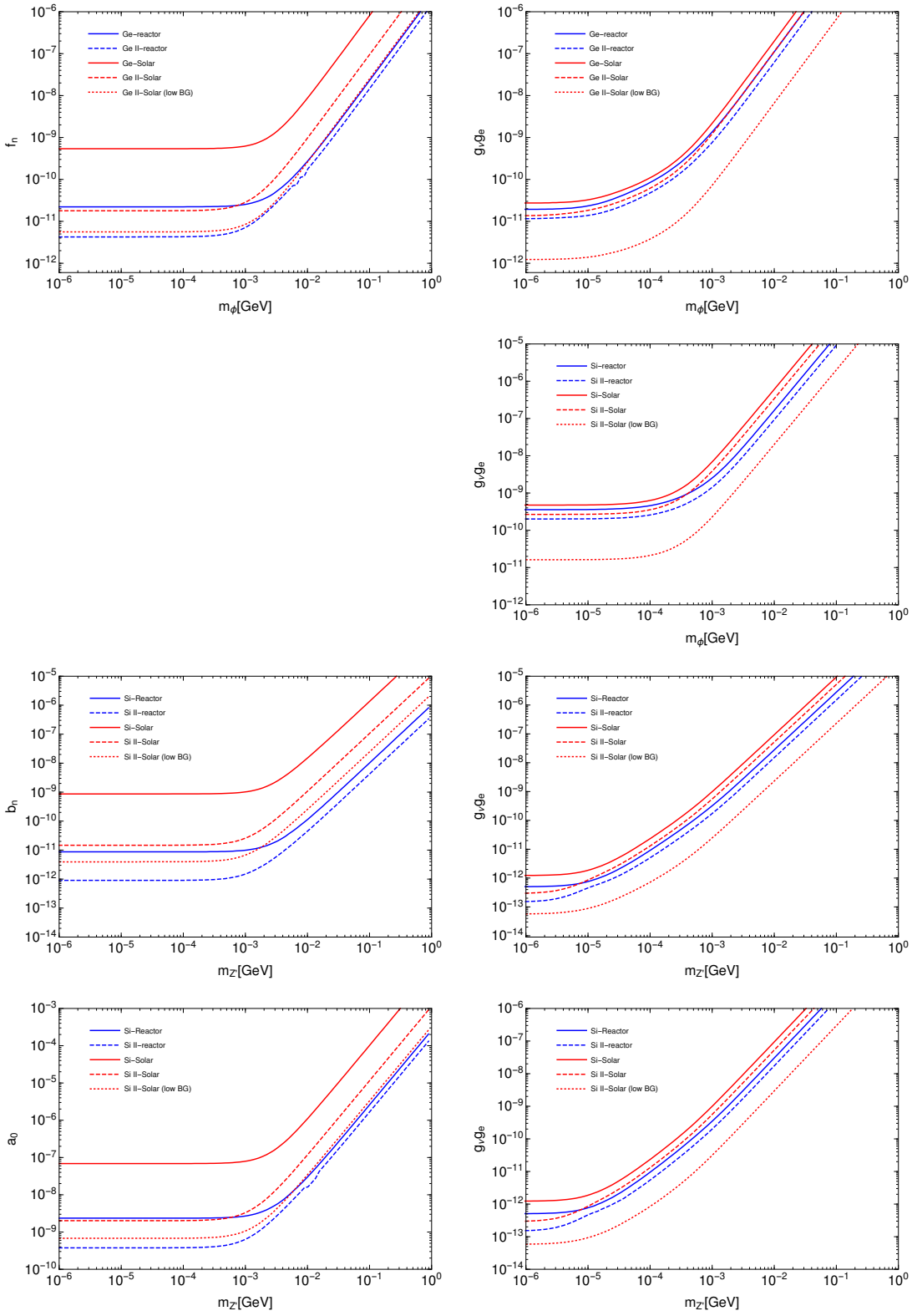


Figure 2.2: The same as Figure. 2.1 but for silicon detectors. Reprinted with permission from [7].

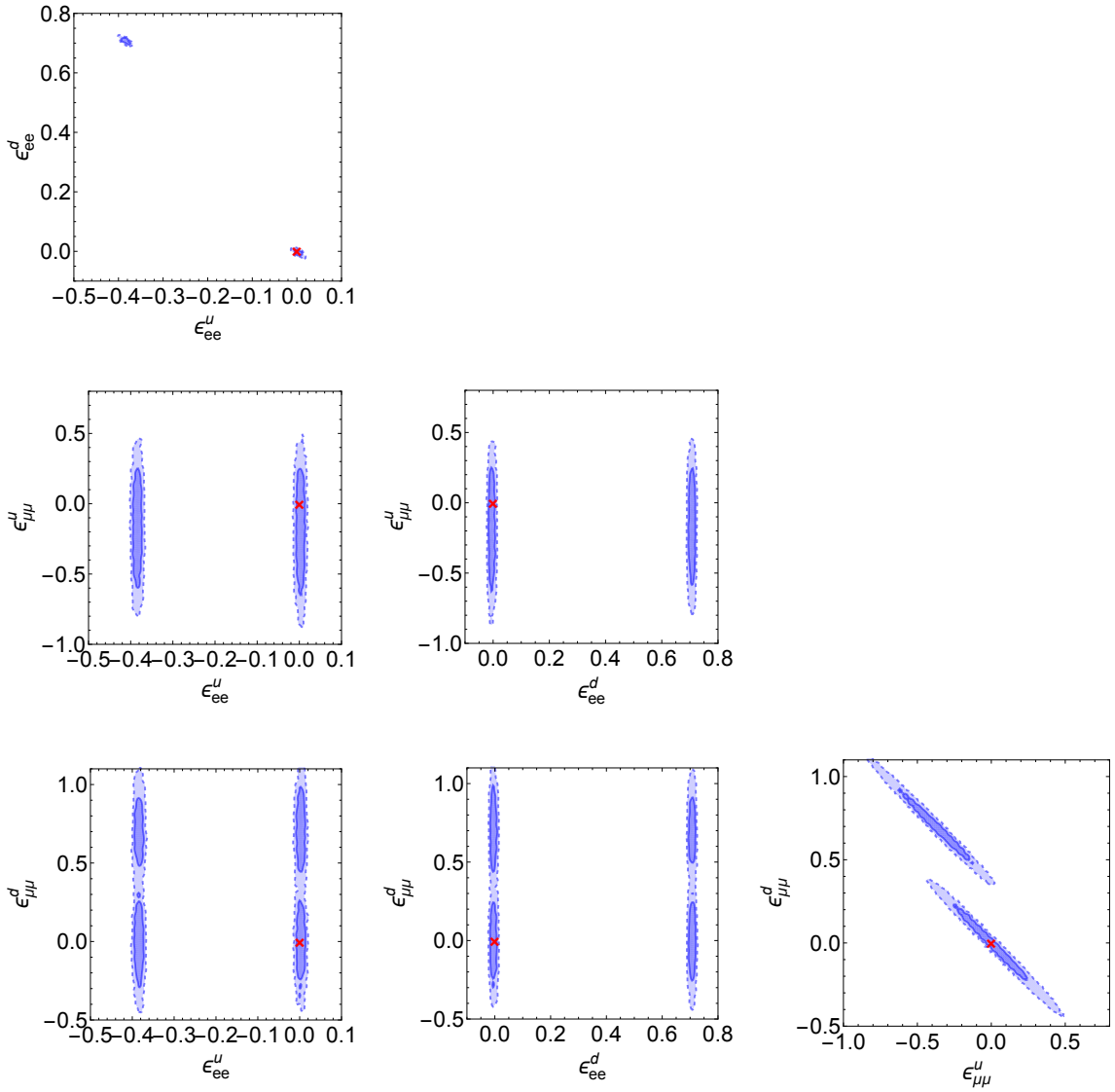


Figure 2.3: Projected posterior probabilities of the four NSI parameters with future accelerator and reactor data. Here we have marginalized over the uncertain experimental backgrounds and fluxes from the respective neutrino sources. The contours show the 68% and 95% credible regions, and the red cross indicates the simulated Standard Model value. Reprinted with permission from [8].

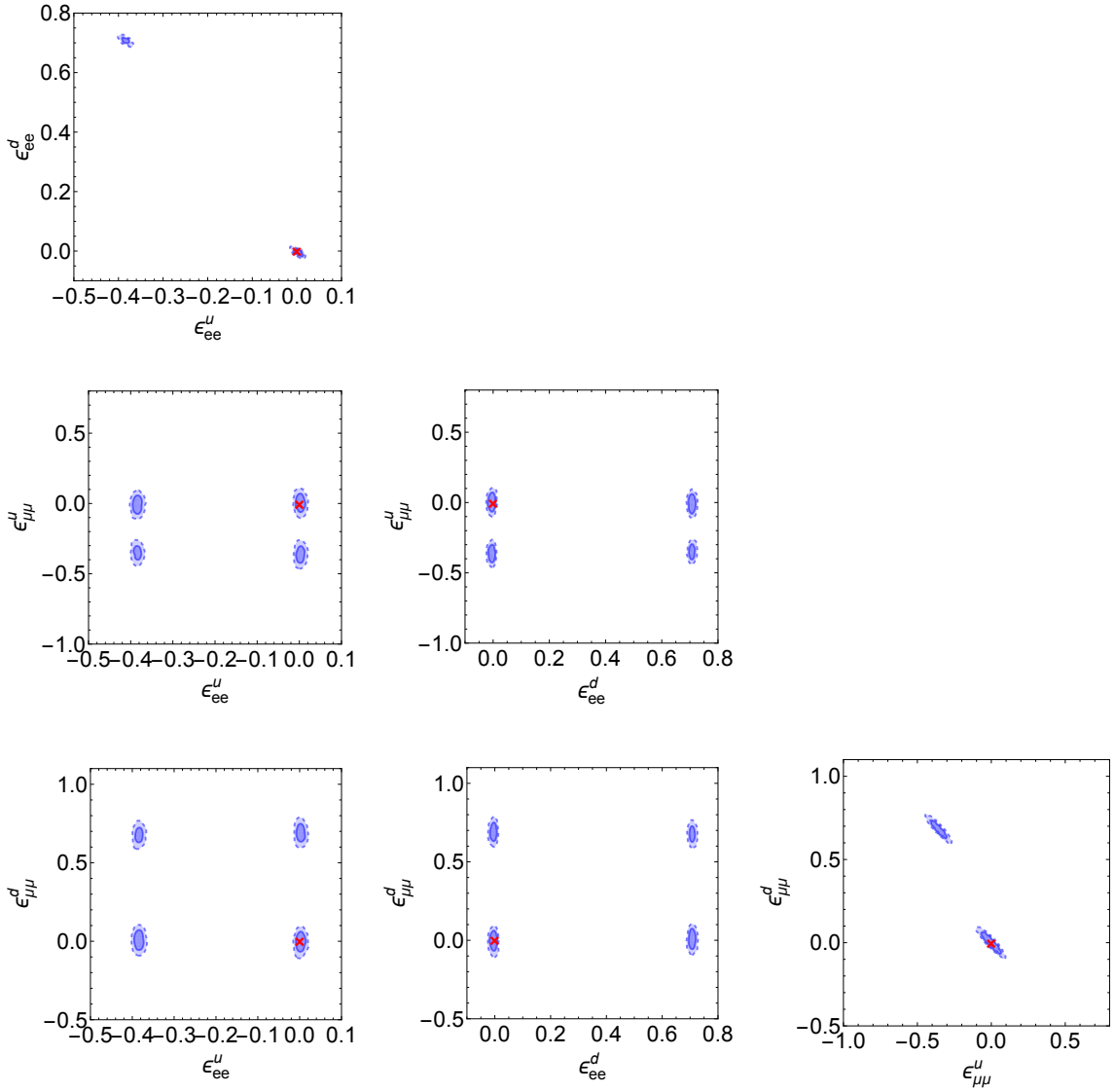


Figure 2.4: Projected posterior probabilities of the four NSI parameters with future accelerator and reactor data. Here we assume zero experimental background for the accelerator detectors, all other uncertainties are marginalized over. The contours show the 68% and 95% credible regions, and the red cross indicates the simulated Standard Model value. Reprinted with permission from [8].

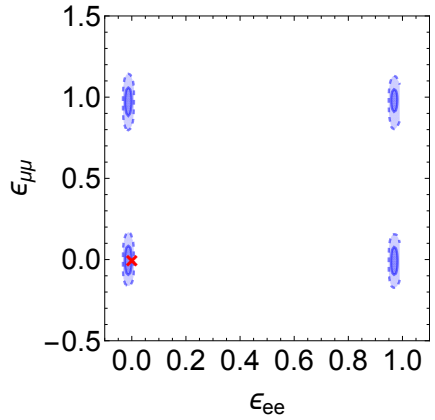


Figure 2.5: Projected posterior probabilities of effective NSI with future accelerator and reactor data, allowing for four flavor diagonal parameters to be non-zero. The contours show the 68% and 95% credible regions, and the red cross indicates the simulated Standard Model value. Reprinted with permission from [8].

## 2.4 Conclusion

In this chapter we have examined the effect of new, light mediating particles on both the CE$\nu$NS process as well as electron scattering by neutrinos, by employing a simplified model approach including new scalar, pseudo-scalar, vector, and axial-vector mediators with sub-GeV masses. Such low mass mediators can create a substantial enhancement in the rate of CE$\nu$NS and $\nu - e$ scattering at low recoil energies, further motivating the continued push towards low threshold detector technology. Furthermore, we showed that the ability of CE$\nu$NS experiments to break down the degeneracies of NSI parameterization of neutrino interactions. We also introduced the multi-parameter Bayesian analysis, which turns out to be particularly useful for analyzing multi-parameter models, and we will use this frame work extensively in later chapters.

# 3. MODELS THAT INDUCE TO NON-STANDARD INTERACTIONS*

In the previous chapter, we discussed the general non-standard interaction of neutrinos and how CE$\nu$NS experiments will act an extraordinary probe of these kind of interactions. Giving the sensitivity to the general NSIs, we can further investigate the experimental reach of more specific models that beyonds SM.

In this chapter, we discuss two well motivated extension of SM: the kinetic mixing effects and hidden sectors that induce $q^2$ form factor in the scattering amplitude. We first discuss the context and formalism of these two extensions of SM; and then analyze the models using current and future(projected) CE$\nu$NS experiments result with $\chi^2$ statistical techniques; finally we draw our conclusion.

## 3.1 Kinetic and mass mixing effects

Kinetic and mass mixing effects can arise from a straight forward $U(1)$ extension of SM model. Many theoretical and phenomenological studies can give rise to such $U(1)$ extension, for example, grand unified theories [25], string theory [26], and solutions to B anomalies [27]. Given such a gauge group with gauge field $Z'$ and field strength $F'_{\mu\nu}$, matter content that is charged under both this and a SM gauge group will generically lead to kinetic mixing of the form $\epsilon F'_{\mu\nu}F^{\mu\nu}$ where $F_{\mu\nu}$ denotes a SM field strength and $\epsilon$ parametrizes the strength of the mixing. This, in turn, can lead to $Z'$ interactions with SM fermions whose nature depends on the details of the model and can be explored by a variety of experiments. A similar result is obtained if a mass mixing with the SM

*Parts of this section are reprinted with permission from:

M. Abdullah, J. B. Dent, B. Dutta, G. L. Kane, S. Liao, and L. E. Strigari, "Coherent elastic neutrino nucleus scattering as a probe of a Z through kinetic and mass mixing effects," *Phys. Rev.* **D98** no. 1, (2018) 015005, `arXiv: 1803.01224 [hep-ph]`. Published by the American Physical Society under the terms of the Creative Commons Attribution 4.0 International license

A. Datta, B. Dutta, S. Liao, D. Marfatia, and L. E. Strigari, "Neutrino scattering and B anomalies from hidden sector portals," *JHEP* **01**(2019) 091, `arXiv: 1808.02611 [hep-ph]`. Published by Springer under the terms of the Creative Commons Attribution 4.0 International license

$Z$ is instead generated. While both $\epsilon$ and the $Z'$ mass, $m_{Z'}$, vary depending on the model, much of the recent work has been focused on a range of $10^{-6} \lesssim \epsilon \lesssim 10^{-2}$ with $m_{Z'} \lesssim 10$ GeV.

We start with a dark Abelian gauge group $U(1)_X$ minxed with SM hypercharge gauge group $U(1)_Y$:

$$L_{gauge} = -\frac{1}{4}F_a^{\mu\nu}F_{a\mu\nu} - \frac{1}{4}F_b^{\mu\nu}F_{b\mu\nu} - \frac{\epsilon}{2}F_a^{\mu\nu}F_{b\mu\nu} \tag{3.1}$$

where $a$ denotes $U(1)_X$ and $b$ denotes $U(1)_Y$, and $\epsilon$ is the mixing strength between the two $U(1)$s. The exact form of the Lagrangian after spontaneous symmetry break where the gauge field is re-diagonalized depends on the Higgs field [28]. In this work, we assume an additional Higgs singlet $\phi_H$ with couplings to the additional $U(1)_X$. After the breaking of $SU(2) \times U(1)_Y \times U(1)_X$, the mass eigenstate $A$, $Z$, and $Z'$ can be expressed in terms of $B_\mu$, $W_\mu^3$ and $X_\mu$ by the following transformation matrix:

$$\begin{pmatrix} B_\mu \\ W_\mu^3 \\ X_\mu \end{pmatrix} = \begin{pmatrix} \cos\theta_w & -\epsilon\,\sin\alpha - \sin\theta_w\cos\alpha & \sin\theta_w\sin\alpha - \epsilon\,\cos\alpha \\ \sin\theta_w & \cos\theta_w\cos\alpha & -\cos\theta_w\sin\alpha \\ 0 & \sin\alpha & \cos\alpha \end{pmatrix} \begin{pmatrix} A_\mu \\ Z_\mu \\ Z'_\mu \end{pmatrix} \tag{3.2}$$

where $\alpha$ arises from the breaking of the new symmetry via the new Higgs singlet. We can then write the $Z'$-fermion-antifermion coupling as:

$$\frac{-ig}{\cos\theta_w}\left[\cos\alpha(\tan\alpha - \epsilon\,\sin\theta_w)\right]\left[T_L^3 - \frac{(\tan\alpha - \epsilon\,/\sin\theta_w)}{\tan\alpha - \epsilon\,\sin\theta_w}\sin^2\theta_w Q\right] \tag{3.3}$$

We consider two limits of this general couplings that can be tested by CE$\nu$NS experiments: 1) $\sin\alpha \sim 0$ so the new $Z'$ resembles a hpyercharge gauge boson:

$$ig\tan\theta_w\,(Y_f/2)\,\epsilon_B \tag{3.4}$$

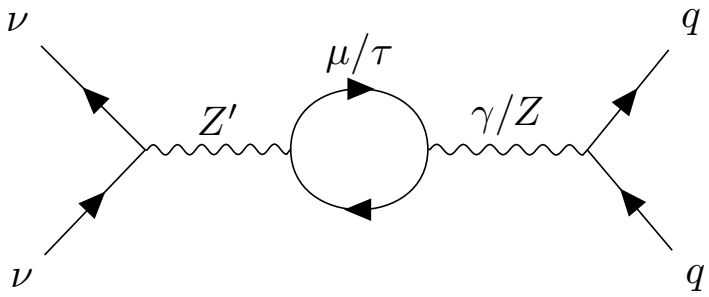


Figure 3.1: Feynman diagram for $L_\mu - L_\tau$ model that generates kinetic mixing.

where $\epsilon_B = \cos\alpha(\tan\alpha - \epsilon \sin\theta_w)$, and we call it dark hypercharge gauge boson; 2) $\epsilon \sim 1$ so the new $Z'$ resembles a $Z$ gauge boson:

$$\frac{-ig}{\cos\theta_w}\,\epsilon_z\,\left[T_L^3 - \sin\theta_w^2 Q\right] \tag{3.5}$$

where $\epsilon_z = \sin\alpha$, and we call it dark $Z$ boson.

Another interesting possibility for probing new physics models is when the SM is extended with a non-universal $U(1)$ gauge symmetry associated with $U(1)_{L_\mu - L_\tau}$. This symmetry has been discussed in various contexts including the flavor structures of neutrinos [29, 30], lepton flavor violating Higgs decays [31], dark matter, and the recently reported flavor non-universality in B decays [32]. This symmetry leads to interactions in the Lagrangian of the form:

$$\mathcal{L}_{int} = g_{Z'} Q_{\alpha\beta}(\bar{l}_\alpha \gamma^\mu l_\beta + \bar{\nu}_{L\alpha}\gamma^\mu \nu_{L\beta}) Z'_\mu \tag{3.6}$$

where, $Z'$ is the new gauge boson, $g_{Z'}$ is the new gauge coupling, and $Q_{\alpha\beta} = \mathrm{diag}(0, 1, -1)$ gives the $U(1)_{L_\mu - L_\tau}$ charges. At low energies, muon and tau loops generate kinetic mixing between the SM photon and $Z'$ of strength $\epsilon = (e g_{Z'})/(6\pi^2)\log(m_\tau/m_\mu)$ via the Feynman diagram shown in Figure 3.1.

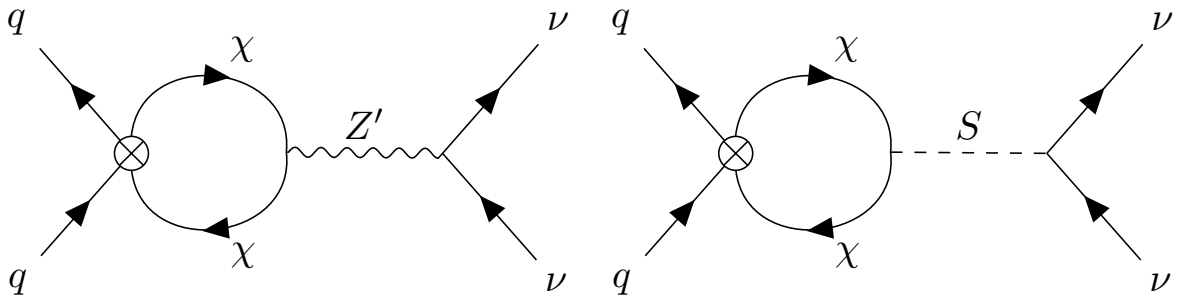


Figure 3.2: Feynman diagram for $Z'$ model (left) and $S$ model (right). Reprinted with permission from [10].

### 3.2 $q^2$ form factors from loop correction

Considering the scenario of $Z^prime$ model where quarks couple to $Z^prime$ via loop of hidden sector particles. We show that this leads to a $q^2/\Lambda^2$ form factor on the $Z'_\mu \bar{q}\gamma^\mu q$ interaction, and how CE$\nu$NS can measure the explanation of $B$ decay anomalies with $q^2$ form factor.

Starting with the following Lagrangian at low energy [33]:

$$\begin{aligned}\mathcal{L} &= \frac{g_{L,R}}{\Lambda^2}\bar{q}\gamma^\mu P_{L,R} q \bar{\chi}\gamma_\mu(1 \pm \gamma_5)\chi + i\bar{\chi}\gamma^\nu\left[\partial_\nu - ig_\chi Z'^\nu\right]\chi - m_\chi\bar{\chi}\chi + \frac{1}{2}m^2_{Z'}Z'_\mu Z'^\mu \\ &= H_{eff} + J_{\mu,\chi}Z'^{,\mu} + i\bar{\chi}\gamma^\nu\partial_\nu\chi - m_\chi\bar{\chi}\chi + \frac{1}{2}m^2_{Z'}Z'_\mu Z'^\mu \end{aligned} \tag{3.7}$$

where $\chi$ is a hidden sector fermion field with mass $m_\chi$. The first term in the Lagrangian represents an effective coupling between the $q$ and $\chi$ fields that might arise through the exchange of a heavy mediator of mass $\sim \Lambda$, with $\Lambda \gg E$, where $E$ is the energy scale of the process. The hidden sector fields $\chi$ couple directly to $Z'$ through the vector portal and so in our framework there are two mediators. We further assume that the neutrinos are charged under the $U(1)'$ and so there is a direct coupling of the neutrinos to $Z'$. The coupling between $Z'$ and quarks can be induced by a loop of hidden sector $\chi$, as shown in Figure 3.2.

We write the induced $Z'_\mu \bar{q}\gamma^\mu q$ interaction as:

$$\mathcal{L}_{int} = \bar{q}\gamma^\mu \left[P_L F_L(q^2) + P_R F_R(q^2)\right] q Z'_\mu \tag{3.8}$$

In one loop approximation we can calculate the form factor [34]:

$$\begin{aligned} F_{L,R}(q^2) &= \frac{q^2}{\Lambda^2}\left[g_{L,R} + \frac{g g_\chi}{2\pi^2}\int_0^1 dx\ x(1-x)\ln\frac{x\Lambda_c^2}{\Delta}\right], \\ &= \frac{q^2}{\Lambda^2} g_{L,R}(\Lambda_c^2) \end{aligned} \tag{3.9}$$

where $\Lambda_c$ is the cut-off to regulate the divergence. As discussed in previous chapter, in CE$\nu$NS experiments, only vector component of the interaction can be probed. So we define the effective Lagrangian as:

$$\mathcal{L}_{int} = \frac{q^2}{\Lambda^2} g' \bar{q}\gamma^\mu q Z'_\mu \tag{3.10}$$

where $g' = g_L(\Lambda_c^2) + g_R(\Lambda_c^2)$ is the effective coupling interested in this chapter.

Similarly, we can also have scalar as mediator instead of vector $Z'$, as shown in Figure 3.2. The effective Lagrangian with $q^2$ form factor is:

$$\mathcal{L}_{int} = \frac{q^2}{\Lambda^2} g'_s \bar{q} q S \tag{3.11}$$

where $g'_s = g_s + \frac{3 g g_\chi}{4\pi^2}\int_0^1 dx\ x(1-x)\frac{\left[m_\chi^2 - q^2 x(1-x)\right]}{q^2\Lambda^2}\ln\frac{x\Lambda_c^2}{\Delta}$. We consider the case $m_\chi^2 \ll q^2$ so that $g'_s$ is $q^2$ independent.

### 3.3 Results and analysis

In each of the models discussed above, there is only one parameters. So it is better suited for a profile-likelihood analysis. According to Wilks' theorem, Equation 2.26 approximate to $\chi^2$ distribution, we can further simplify the analysis by using the $\chi^2$

method. We define:

$$\chi^2 = \sum_{\text{bins,detectors}} \frac{\left(N_{exp} - (1+\beta)\, N_{pred}\right)^2}{N_{bg} + N_{exp}} + \left(\frac{\beta}{\sigma_\beta}\right)^2 \tag{3.12}$$

where $N_{exp}$ is the expected number of events in the SM (or the observed number of events in the case of current COHERENT limits), $N_{pred}$ is the number of predicted events in our model, $N_{bg}$ is the number of background events, $\sigma_\beta$ is the fractional systematic uncertainty, and $\beta$ is the corresponding nuisance parameter. The current COHERENT experiment has a threshold 4.25 keV [5]. For the future projected measurements we assume a threshold of 100 eV for Ge and Si reactor experiments [35–37], and 2 keV for NaI and Ar with COHERENT [38]. For reactor neutrinos we take a background of 1 dru (Ge and Si), and for accelerator neutrino data we take a background of $5 \times 10^{-3}$ dru (CsI, NaI and Ar) [5]. Here the unit dru stands for differential rate unit, equal to event/ (keV $\cdot$ kg $\cdot$ day). The COHERENT experiment has an energy dependent efficiency. We applied the efficiency function from [5] to all the detectors in the COHERENT experiment. We take the reactor neutrino flux to be that of a 1 MW reactor at $\sim$ 1 m from the core (which yields a the total flux of $1.5 \times 10^{12}$ cm$^2$/s), and the antineutrino fission spectrum at various sites from Ref. [39]. The accelerator neutrino flux at SNS is $4.29 \times 10^9$ cm$^2$/s [5].

### *3.3.1 Current and future bounds on mixing parameters*

First we show the current and future bounds on dark hypercharge mixing and dark $Z$ mixing scenario in Figure 3.3 comparing to limits from fixed target, atomic parity violation experiments and the BaBar results. We find limits that are complementary to those from fixed target experiments. For these scenarios, however, the atomic parity violation experiment provides the best constraint for a large region of parameter space. The Babar results provide better constraints for $m_{Z'} \sim 10$ GeV. In typical string/M-theory based models, it is argued that $\epsilon \sim 10^{-1} - 10^{-3}$ [40] where hypercharge mixing

is considered. Based on Figure 3.3, we can see that most of the parameter space for these models is ruled out. However, it is also argued in the context of LVS (Large Volume Scenario) that $\epsilon \sim 10^{-6} - 10^{-8}$, which survives the experimental constraint. In such models, the dark matter candidate in the visible sector decays into hidden sector particles via 2 and 3 body decay modes and the lifetime depends on $\epsilon$. The restriction on $\epsilon$ from our analysis constrains the lifetime of the dark matter particle into 3-body and 2-body decay modes to be $10^{-10} - 10^{-13}$ sec and $10^{-18} - 10^{-21}$ sec, respectively, where these ranges correspond to a $Z'$ mass spanning $10^{-3} - 10$ GeV.

One interesting aspect of the dark $Z$ case is the limits seem to be independent of exposure at large mediator mass. This can be explained by examine the $\chi^2$ method in Equation 3.12. After maximizing the expression with respect to the nuisance parameter $\beta$ and defining $k \equiv \frac{N_{pred}}{N_{bg}+N_{exp}}$, we get:

$$\chi^2 = \frac{-\left(\sum \frac{N_{pred}N_{exp}}{N_{bg}+N_{exp}}\right)^2 + \sum \frac{N_{pred}^2}{N_{bg}+N_{exp}} \sum \frac{N_{exp}^2}{N_{bg}+N_{exp}} + \frac{1}{\sigma^2} \sum \frac{\left(N_{pred}-N_{exp}\right)^2}{N_{bg}+N_{exp}}}{\frac{1}{\sigma^2} + \sum \frac{N_{pred}^2}{N_{bg}+N_{exp}}} \tag{3.13}$$

$$\simeq \sum \frac{N_{exp}^2}{N_{bg}+N_{exp}} - \frac{\sum kN_{exp}}{\sum kN_{pred}} \sum kN_{exp} \tag{3.14}$$

where in the second line we used the fact that $1/\sigma^2$ is small compared to $N_{exp}$. As mentioned earlier, the $Z'$ coupling relative to the $Z$ coupling is universal in the dark $Z$ scenario which means that $k$ is the same for all detectors and energy bins at the high $M_{Z'}$ region. Therefore, Equation 3.14 can be solved for $k$ to give

$$k = \left(\sum \frac{N_{exp}^2}{N_{bg}+N_{exp}} - \chi^2\right) / \sum N_{exp} \simeq \left(\sum \frac{N_{exp}^2}{N_{bg}+N_{exp}}\right) / \sum N_{exp}. \tag{3.15}$$

In other words, $k$, and hence $\epsilon_Z$ is independent of the exposure. This argument breaks down for the dark hypercharge case due to the detector dependence on $k$.

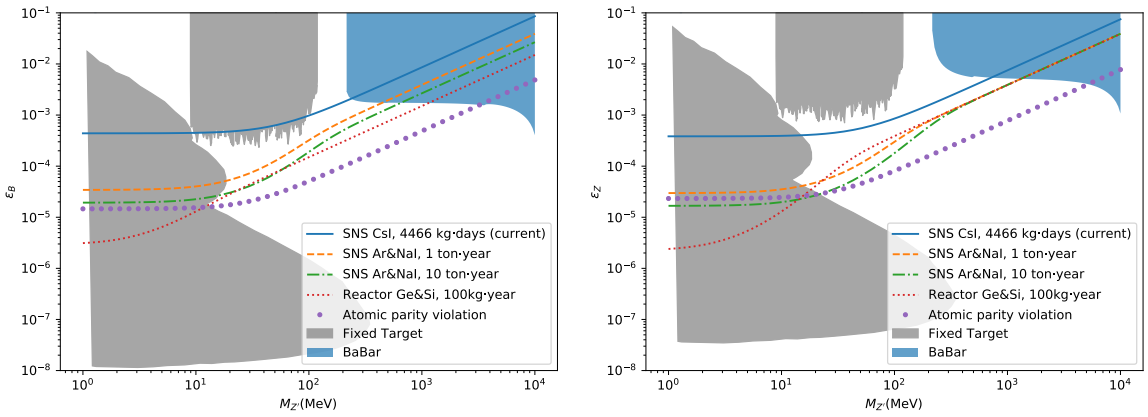


Figure 3.3: The current and future bounds on the mixing $\epsilon_B$ in the dark hypercharge case (left) and minxing $\epsilon_Z$ in the dark $Z$ case (right) are plotted as a function of the $Z'$ mass $M_{Z'}$. The solid blue curve is the current COHERENT limit, the orange dashed and green dot-dashed curves are derived future projections for COHERENT for different luminosities, the red dotted curved is the future projection for a reactor experiment, the purple large-dotted curve is from atomic parity violation, the grey regions are from the NA48/2, E774, E141, and E137 fixed target experiments. The blue shaded region is diallowed by the BaBar results. Reprinted with permission from [9]

In Figure 3.4 we show the limits on the induced mixing case by $L_\mu - L_\tau$ model. We compare current and projected COHERENT results to the limits from Borexino, CCFR, and Babar. We find the COHERENT, Borexino and CCFR complement each other, with COHERENT provide strongest limits in $4\,\text{MeV} \lesssim m_{Z'} \lesssim 100$ mass window. We do not show reactor limits because it require electron flavor couplings. With same reason, Barbar, fixed target and atomic parity violation experiments have poor limits in this scenario.

### *3.3.2 Current and future bounds of NSI coupling with $q^2$ form factor*

We show the current and projected result on the limit in the presence of $q^2$ form factor and compare to the coupling without form factor in Figure 3.5. To compare the couplings a factor of $q^2/\Lambda^2$ is multiplied so that $\frac{g'q^2}{\Lambda^2}$ represents the coupling strength between quarks and neutrinos as a function of energy and reduces to $g'$ if there is

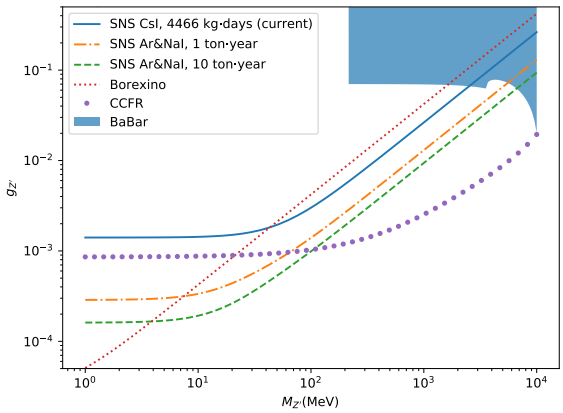


Figure 3.4: The current and future bounds on the coupling $g_{Z'}$ in the $L_\mu$-$L_\tau$ model are plotted as a function of the $Z'$ mass $M_{Z'}$. The solid blue curve is the current COHERENT limit, the orange dot-dashed and green dashed are derived future projections for COHERENT for different luminosities, the red dotted curve is from the Borexino measurement of solar neutrinos, and the purple large-dotted curve is from the CCFR measurement of neutrino trident production. The blue shaded region is ruled out by the BaBar results. Reprinted with permission from [9]

no form factor for the coupling. We choose $q_0$ to be a typical momentum for the experiment, e.g., $q_0 = 50$ MeV and 30 MeV are used for COHERENT and reactor experiments, respectively. The limits on the coupling strength with form factor is typically stronger than that without form factor, as can be seen from figure 3.5. This is because with $q^2$ form factor, the spectral shape will be differ from the SM prediction, while without $q^2$ new spectral will be the same. As a result, we can use binning analysis of the data to extract more information on the spectral. We illustrate this in Figure 3.6. The main difference between the solid lines and dashed lines are at the higher energy end because the form factor $q^2$ enhances the deviation from the SM. At low energy, the spectrum is suppressed by the detection efficiency.

With typical momentum transfer $\sim 0.4$ MeV, Solar neutrino is able to probe much smaller value of $\Lambda$ as compared to reactor and accelerator CE$\nu$NS experiments. Here we consider all the most prominent low energy components of the solar neutrino flux that Borexino is sensitive to, i.e., *pp*, *pep*, and $^7$Be. We choose the high metallicity

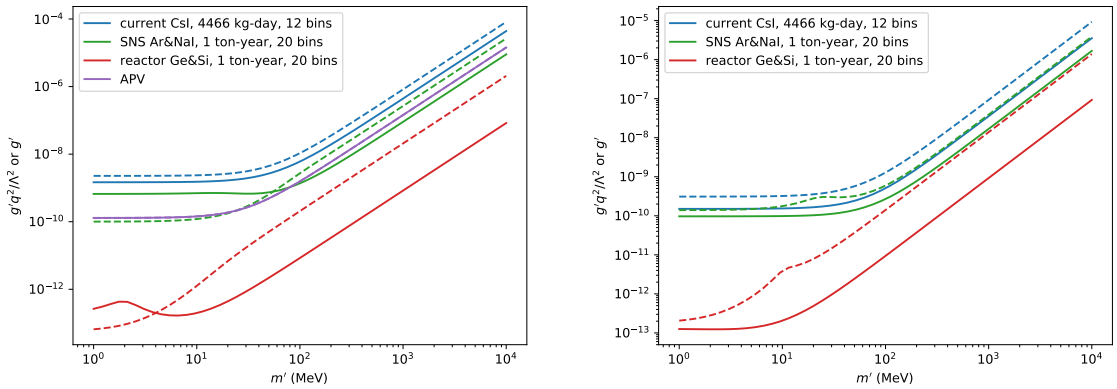


Figure 3.5: Current and projected $2\sigma$ bounds on a vector(left) or scalar(right) mediator with $F(q^2) \sim q^2$ as a function of the mediator mass. Dashed lines show the limits without a form factor. Here $q_0 = 50$ MeV for COHERENT, and $q_0 = 30$ MeV for reactor experiments. Reprinted with permission from [10]

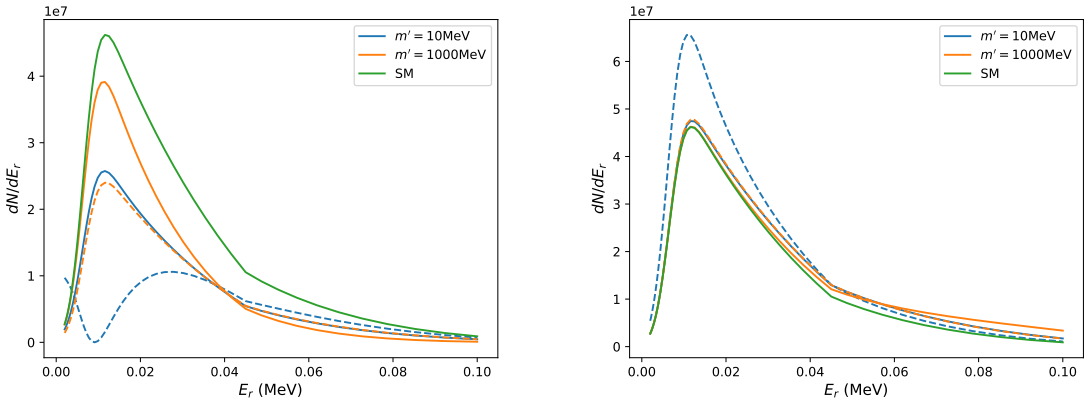


Figure 3.6: Spectrum of neutrino scattering off Ar detector with 1 ton−year exposure, with $\Lambda = 100$ MeV. The left panel is for the vector mediator and the right panel is for the scalar mediator. Here the couplings for non-standard interactions are taken from the bound of current COHERENT CsI limit. The dashed lines show the spectrum without a form factor. Reprinted with permission from [10]

solar model as defined in Ref. [23] for our baseline Standard Solar Model (SSM), and comment on the impact of the model uncertainties below.

For solar neutrino experiments, the systematic uncertainties dominate. So we define $\chi^2$ for each component of the solar flux to be

$$\chi^2 = \frac{(N_{th} - N_{obs})^2}{N_{obs}\sigma}\,, \tag{3.16}$$

where $\sigma$ is the percent uncertainty in the measurement (including experimental and theoretical uncertainties in quadrature) with $\sigma_{pp} = 0.11$, $\sigma_{^7Be} = 0.03$, and $\sigma_{pep} = 0.21$ [41]. To obtain a combined limit we define $\chi^2 = \chi^2_{pp} + \chi^2_{^7Be} + \chi^2_{pep}$.

In Figure. 3.7, we show the constraints on the $ee\nu\nu$ coupling from Borexino [41]. We find that the *pp* and $^7Be$ components provide the strongest constraints on $F(q^2) \sim q^2$ because of their higher event rates and smaller flux uncertainties. This is despite the fact that the *pep* component has larger spectral distortions (for the form-factor case relative to the $F(q^2) = 1$ case) due to its higher energy. The limit plots are valid as long as $\Lambda^2 \gg q^2$.

As for the nucleus scattering case, the recoil spectra in Fig. 3.8 show that the $F(q^2) \sim q^2$ case is different from the $F(q^2) = 1$ case. We see that the major differences in the spectra are at high energies. The differences for the scalar case are more significant than for the vector case because in the vector scenario the $q^2$ enhancement is suppressed by the interference between SM and new physics contributions.

### 3.4 Conclusion

In this chapter, we have discussed two specific realization of non-standard interaction of neutrino: kinematic mixing and $q^2$ form factor arising from loops of hidden sector. CE$\nu$NS experiments give either better constraints on the model or profound discoverability of the model parameters.

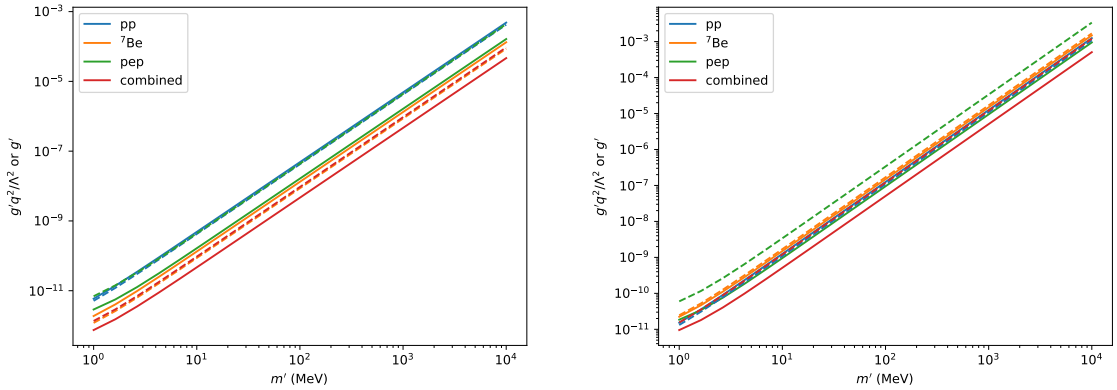


Figure 3.7: Constraints at $2\sigma$ from the Borexino experiment on a vector(left) or scalar(right) mediator with $F\left(q^2\right) \sim q^2$ as a function of the mediator mass, compared to the case of a mediator without a form factor (dashed line). We set $q = 0.5$ MeV and $\Lambda = 10$ MeV for the form factor case to compare it to the no-form-factor case. Reprinted with permission from [10]

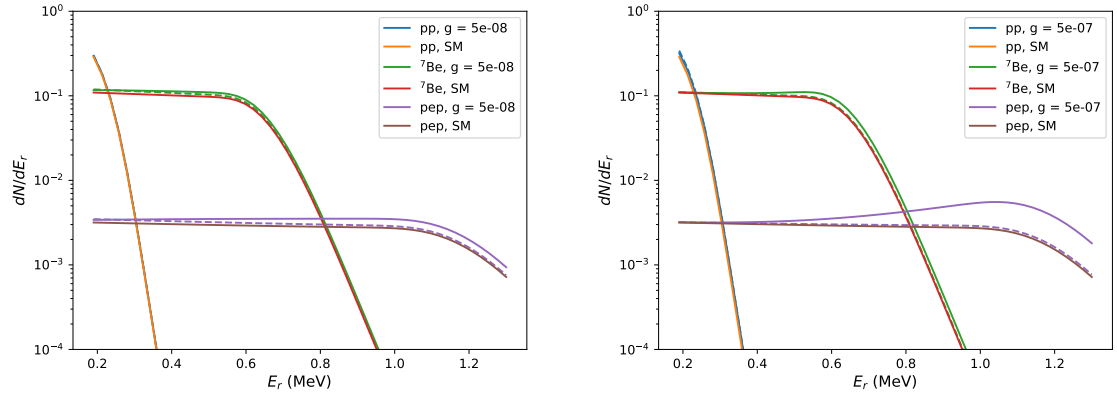


Figure 3.8: Spectra of solar neutrino scattering off electrons, with $m' = 10$ MeV and $\Lambda = 10$ MeV, and scaled to match the Borexino measurement. The left panel is for the vector mediator and the right panel is for the scalar mediator. Dashed lines are the spectra without a form factor. To make a fair comparison, for the latter case we scale $g$ by a factor of $q^2/\Lambda^2$. Reprinted with permission from [10]

# 4. DIRECT DARK MATTER DETECTION AS NEUTRINO EXPRIMENTS*

Apart from dedicated neutrino experiments for CE$\nu$NS discussed in the previous chapters, direct detection of dark matter experiments can also play important roles as CE$\nu$NS experiments. The signals from the sun, supernovae, and atmospheric neutrinos will be major contributions to the direct dark matter search experiments, know as neutrino floor [42]. Understanding the neutrino background will not only help the dark matter detection experiment itself, but also it provides an excellent source of information to understand neutrino physics.

In this chapter, we consider future direct dark matter detection experiments as probes of non-standard interactions of neutrinos, specifically, solar neutrinos. We focus on solar neutrinos because their flux has been well studied and their interaction rates can be readily compared to the corresponding rates deduced from previous experiments. We consider interactions between all types of neutrino flavors and fermions, and use a three-flavor formalism accounting for NSI in propagation through the solar interior and in detection on Earth. For detection, we consider both elastic neutrino-electron scattering and coherent neutrino-nucleus scattering, and show that these channels are complementary, probing distinct regimes of the NSI parameter space.

We identify a range of NSI parameter space that is not ruled out by neutrino experiments, but is observable in dark matter experiments. For certain parameters, we show that due to NSI the event rate can be either enhanced or decreased relative to the SM value. For rates which are increased, we identify parameter ranges that can be probed by forthcoming ton-scale direct dark matter detection experiments [12, 43].

*Parts of this section are reprinted with permission from:

B. Dutta, S. Liao, L. E. Strigari, and J. W. Walker, "Non-standard interactions of solar neutrinos in dark matter experiments," *Phys. Lett.* **B773** (2017) 242-246, `arXiv: 1705.00661 [hep-ph]`. 

We identify an interference range of NSI parameters for which the rate is reduced by approximately 40%. We additionally show that the "dark side" solution for solar neutrino mixing angles can be probed by forthcoming dark matter experiments.

### 4.1 Neutrino oscillation and matter effects

The solar neutrino detection is different from reactor or beam based neutrino experiments discussed in previous chapter, because solar neutrino travels a long distance to earth. As a result, in the propagation, different flavors of neutrino will mix with each other. The NSI will affect the oscillation by participating the matter effect in the solar neutrino propagation. To describe the neutrino oscillation and matter effects, first consider the propagation of neutrino in the vacuum; it is described by Schrödinger equation in mass eigenstate:

$$\begin{aligned} i\frac{\mathrm{d}}{\mathrm{d}t}\left|\nu_i\right\rangle &= \mathcal{H}_{ij}\left|\nu_j\right\rangle \\ &= \begin{pmatrix} \sqrt{m_1^2+p^2} & 0 & 0 \\ 0 & \sqrt{m_2^2+p^2} & 0 \\ 0 & 0 & \sqrt{m_3^2+p^2} \end{pmatrix}\left|\nu_i\right\rangle \\ &= \begin{pmatrix} p+\frac{m_1^2}{2p} & 0 & 0 \\ 0 & p+\frac{m_2^2}{2p} & 0 \\ 0 & 0 & p+\frac{m_3^2}{2p} \end{pmatrix}\left|\nu_i\right\rangle \end{aligned} \tag{4.1}$$

Since the constant does not affect the probability, Equation **??** can be written as

$$i\frac{\mathrm{d}}{\mathrm{d}t}\left|\nu_i\right\rangle = \begin{pmatrix} 0 & 0 & 0 \\ 0 & \frac{\Delta m_{21}^2}{2E} & 0 \\ 0 & 0 & \frac{\Delta m_{31}^2}{2E} \end{pmatrix}\left|\nu_i\right\rangle \tag{4.2}$$

Just like CKM matrix, we can transform mass eigenstate to flavor eigenstate via a

transforming matrix:

$$U = R_{-23} T_\delta R_{13} T_{-\delta} R_{-12} \tag{4.3}$$

where $R$ is the rotation matrix, $T_\delta = \begin{pmatrix} 1 & & \\ & 1 & \\ & & e^{i\delta} \end{pmatrix}$.

The Hamiltonian induced by interaction with matter is

$$\mathcal{H}_{\text{int}} = -\mathcal{L}_{\text{int}} = -2\sqrt{2} G_F \theta^P_{\alpha\beta} \bar{\nu^\alpha_L} \gamma^\mu \nu^\beta_L \bar{f}_P \gamma^\mu f_P \tag{4.4}$$

averaging over the matter:

$$\begin{aligned} \langle \mathcal{H}_{\text{int}} \rangle &= -\sqrt{2} G_F \bar{\nu^\alpha_L} \gamma_\mu \nu^\beta_L \int \frac{\mathrm{d}^3 p}{(2\pi)^3 2p^0} \frac{1}{2} \sum_s \langle p, s | \theta^V_{\alpha\beta} \bar{f} \gamma^\mu f + \theta^A_{\alpha\beta} \bar{f} \gamma^\mu \gamma^5 f | p, s \rangle \\ &= -\sqrt{2} G_F \bar{\nu^\alpha_L} \gamma_\mu \nu^\beta_L \int \frac{\mathrm{d}^3 p}{(2\pi)^3 2p^0} \frac{1}{2} \left\{ \theta^V_{\alpha\beta} \mathrm{tr} \left[ \left( -\not{p} + m_f \right) \gamma^\mu \right] + \theta^A_{\alpha\beta} \mathrm{tr} \left[ \left( -\not{p} + m_f \right) \gamma^\mu \gamma^5 \right] \right\} \\ &= \sqrt{2} G_F \theta^V_{\alpha\beta} n_f \bar{\nu^\alpha_L} \gamma^0 \nu^\beta_L \end{aligned} \tag{4.5}$$

where $n_f = \int \frac{\mathrm{d}^3 p}{(2\pi)^3}$ is the number density of the fermion.

So in flavor eigenstate, the full Schrödinger equation is

$$i \frac{\mathrm{d}}{\mathrm{d}t} |\nu_\alpha\rangle = \left( \left[ U \mathrm{diag} \left( 0, \frac{\Delta m^2_{21}}{2E}, \frac{\Delta m^2_{31}}{2E} \right) U^\dagger \right]_{\alpha\beta} + \sqrt{2} G_F \sum_f n_f \left( \delta^{ef} \delta_{e\alpha} + \epsilon^f_{\beta\alpha} \right) \right) |\nu_\beta\rangle \tag{4.6}$$

the $\delta^{ef}\delta_{e\alpha}$ accounts for the charge current interaction with an electron.

We determine the neutrino survival probability in a full three-flavor framework. The survival probability is obtained by diagonalizing the Hamiltonian

$$\mathcal{H}(t) = \tilde{U}(t) \, \mathrm{diag} \left( \frac{m^2_1(t)}{2E}, \frac{m^2_2(t)}{2E}, \frac{m^2_3(t)}{2E} \right) \tilde{U}(t)^\dagger . \tag{4.7}$$

The density in the sun changes smoothly enough that neutrinos propagate adiabatically.

This means that by averaging over the distance, the probability of transition from flavor $\beta$ to flavor $\alpha$ is

$$P_{\beta\to\alpha} = \left|\tilde{U}\left(t\right)_{\alpha i}\right|^2 \left|\tilde{U}\left(0\right)_{\beta i}\right|^2. \tag{4.8}$$

This can be interpreted as the multiplication of the probability of transition to a mass eigenstate at the production region and at the escaping region [44].

We note that previous authors have computed the solar neutrino survival probability including NSI within a reduced two-flavor framework [45]. We find that the two-flavor framework is a good approximation to the full three-flavor framework, with the only discrepancy arising at high neutrino energy, where the approximation that $G_F \sum_f n_f \epsilon^f_{\alpha\beta} \ll \Delta m^2_{31}/E_\nu$ breaks down. In the energy regime where most solar neutrinos lie (eg. $E_\nu < 20\,\mathrm{MeV}$), the three-flavor survival probability in Equation 4.8 will give the same result as the more commonly used two-flavor survival probability. The advantage of adopting the three-flavor oscillation framework is that it enables the examination of entire space of $\epsilon$ using scattering experiments.

### 4.2 Results and analysis

We use the save $\chi^2$ method described in previous chapter to analyze the limits that can be put on the NSI parameter space. The difference between this chapter an previous chapter is here we consider the effects of NSI on both neutrino oscillation and scattering at the same time.

In order to isolate the impact of individual NSI parameters, we allow a given $\epsilon$ to vary one at a time, while keeping all others fixed. For simplicity we just present results for a xenon target, though the salient points of our argument are not affected by this choice. Unless otherwise indicated we take the LMA solution for the neutrino oscillation parameters [46]. For the solar neutrino fluxes, we take the high metallicity standard solar model [23, 47], and we include all the components of the solar spectrum.

We first show in Figure 4.1 how the electron recoil event rate due to elastic scat-

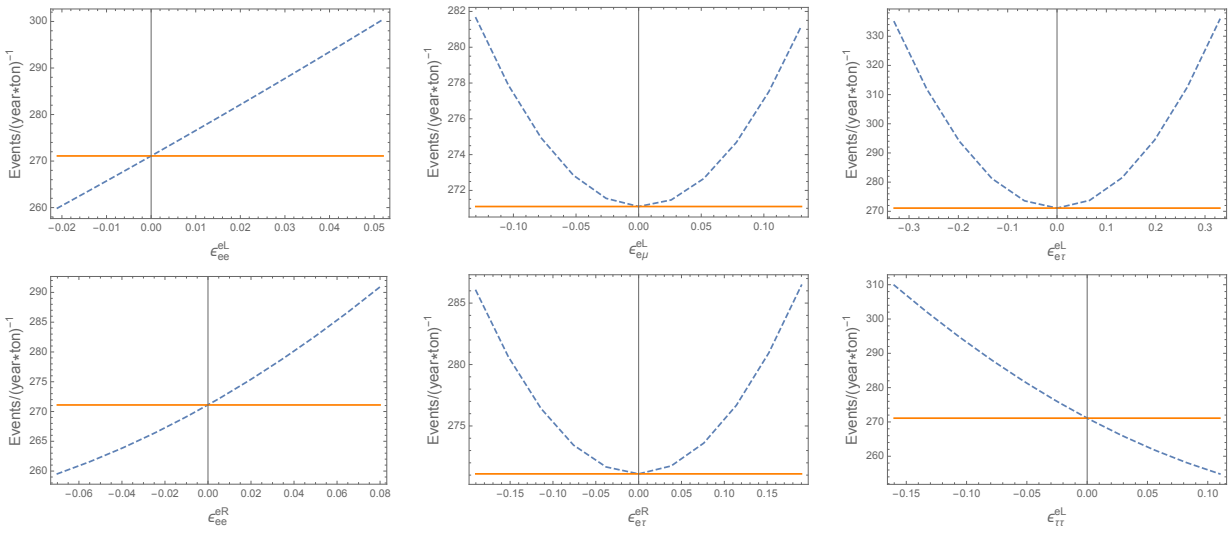


Figure 4.1: Number of events above an equivalent electron recoil energy threshold of 1 keV as each $\epsilon$ varies over its allowable range (dashed blue curves). The solid orange curve gives the SM contribution. Reprinted with permission from [13].

tering, $\nu + e^- \to \nu + e^-$, is affected as each $\epsilon$ varies over their respective allowed range. The electron recoils are primarily due to low energy *pp* solar neutrinos, with a $\lesssim 10\%$ contribution from $^7$Be neutrinos. Depending on the value of $\epsilon$, the event rate may either be greater than or less than the corresponding SM event rate. In large regions of parameter space, we find that the existence of NSI parameters can be distinguished from the SM.

Similarly, we show in Figure 4.2 how the NSI affects the CE$\nu$NS rate. In contrast to the case of electron recoils, in order to get an observable effect, the threshold needs to be relatively low, $\sim$ 1 keV, as the nuclear form factor suppresses the number of events at high energy drastically. Future xenon experiments are expected to be able to achieve the required threshold energies [48].

To quantify how much the matter effect can change the prediction of number recoil events, in Table 4.1, we show the ratio between expected number of events in the presence of NSI to the expected number of events with only SM. We consider the hypothetical scenario where matter effects does not exit and compare to the real case

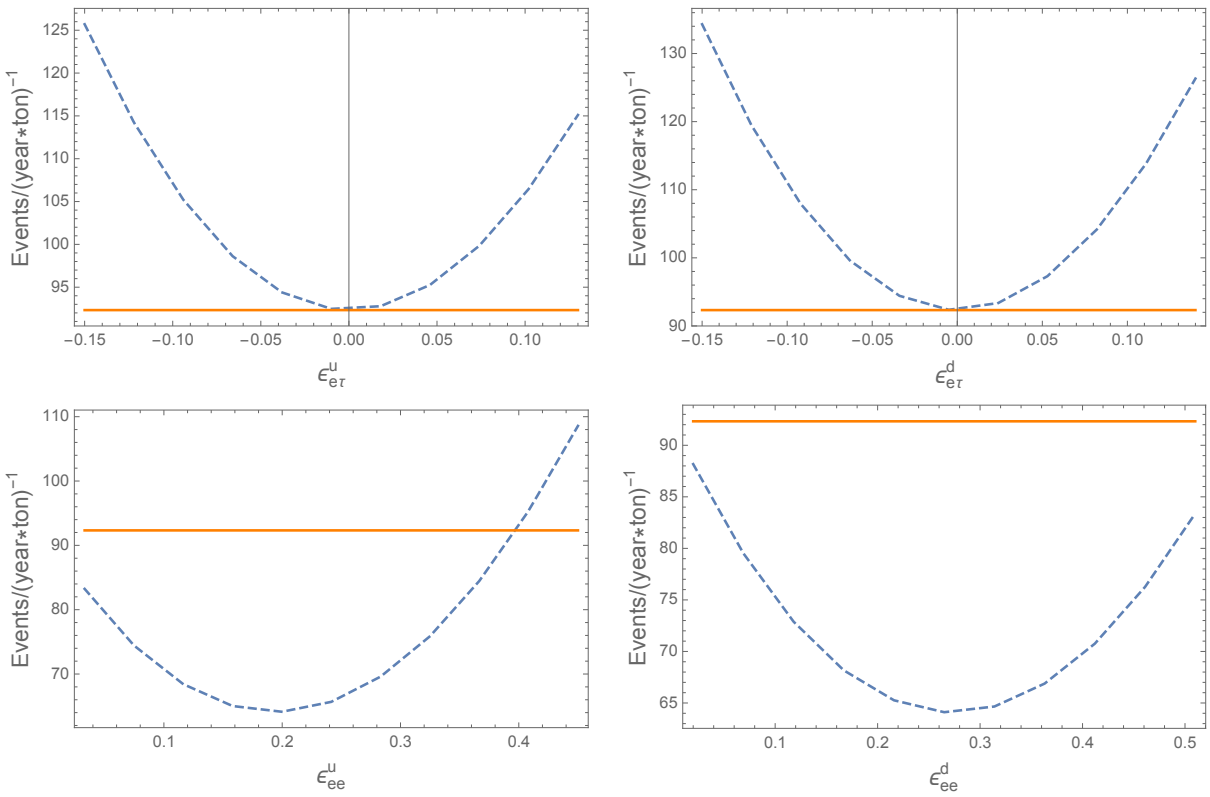


Figure 4.2: Number of events above a nuclear recoil energy threshold of 1 keV as each $\epsilon$ varies over its allowable range (dashed blue curves). The solid orange curve gives the SM contribution. Reprinted with permission from [13].

| | $\epsilon_{ee}^{eL} = 0.052$ | $\epsilon_{e\mu}^{eL} = 0.13$ | $\epsilon_{e\tau}^{eL} = 0.33$ | $\epsilon_{ee}^{eR} = 0.08$ | $\epsilon_{e\tau}^{eR} = 0.19$ | $\epsilon_{\tau\tau}^{eL} = -0.16$ | $\epsilon_{ee}^{u} = 0.2$ | $\epsilon_{e\tau}^{u} = -0.15$ | $\epsilon_{e\tau}^{d} = -0.15$ | $\epsilon_{ee}^{d} = 0.26$ |
|---|---|---|---|---|---|---|---|---|---|---|
| $\frac{N_{MSW}}{N_{SM}}$ | 1.10 | 1.03 | 1.23 | 1.07 | 1.05 | 1.14 | 0.69 | 1.36 | 1.45 | 0.69 |
| $\frac{N_{noMSW}}{N_{SM}}$ | 1.69 | 1.52 | 1.79 | 1.51 | 1.55 | 1.47 | $4 \times 10^{-5}$ | 1.56 | 19.07 | $5 \times 10^{-3}$ |

Table 4.1: Rows 1 and 2 give the ratio of the number of events for a given $\epsilon$, with and without the inclusion of neutrino transformations in Equation 4.7. $N_{SM}$ is the number of events in the SM, without NSI, $N_{MSW}$ is the number of events including NSI in the Hamiltonian, and $N_{noMSW}$ is the number of events without accounting for the MSW term at all. For each column, the $\epsilon$ is chosen to maximize the difference from SM. Reprinted with permission from [13].

when matter effect is changing the neutrino oscillation. Instances in which the ratios $N_{noMSW}/N_{SM}$ and $N_{MSW}/N_{SM}$ are close together implies that the largest impact of NSI comes from the detection cross section in Equation 2.21. Where these ratios are very different, such as with $\epsilon_{ee}^{u}$ and $\epsilon_{ee}^{d}$, the dominant effect of NSI comes from matter-induced transformations.

Finally, we note that when NSI are allowed, a "dark side" solution for the LMA appears, characterized by $\theta_{12} > 45°$ (LMA-d) [49]. Neutrino oscillation experiments alone cannot distinguish this solution from normal solution as the expected signal is same for these two solution. However, with a low threshold dark matter detector, we will be able to distinguish the two solution by counting the observed number of neutrino events. In Figure 4.3, we show that this solution can be discovered in direct detection experiments for threshold energies of 1 keV. Thus forthcoming direct detection experiments have a novel and unique discovery sensitivity to the entire region of the LMA-d solution.

### 4.3 Conclusion

In this chapter, we discussed the possibility of using direct dark matter search experiments as a probe of NSI parameters of neutrino. We discovered that direct dark matter searches are able to probe NSI parameter space that cannot be probed by current neutrino experiments, implying that direct dark matter searches have an important role in searches for beyond the Standard Model physics through the neutrino

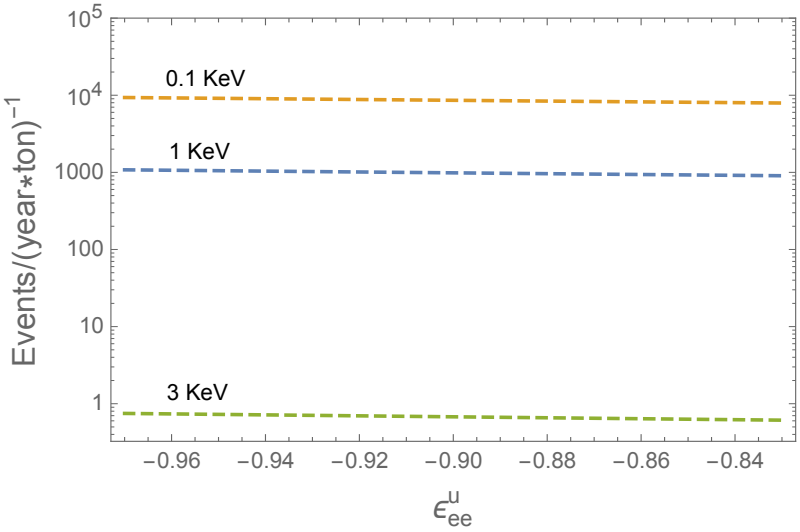


Figure 4.3: Total number of events above an indicated nuclear threshold energy for the LMA-d solution with $\sin^2\theta_{12} = 0.7$ [50], for three different threshold energies. Reprinted with permission from [13].

sector. And the matter effect will alter the prediction of number of events significantly with some NSI parameters, suggesting that solar neutrino in direct dark matter searches supplement the neutrino oscillation experiments.

# 5. ANALYSIS OF COHERENT EXPERIMENT DATA WITH ENERGY AND TIMING INFORMATION*

After COHERENT collaboration reported the first detection of CE$\nu$NS [5], the collaboration released the detailed data with number of events binned in both time and energy dimensions [14]. The data do not directly identify the flavor components of the neutrino flux, though it is possible to make an estimate for the contribution of the different flavors. For example the prompt $\nu_\mu$ component may be estimated from a timing cut, while the delayed components may be extracted from their spectral signatures. Previous authors have classified the events as prompt or delayed using a two-bin analysis in timing space [51].

With full energy and timing distributions of nuclear recoil events provided in the data release, we are able to perform likelihood analysis that utilize informations not available from the energy data alone, or when splitting the timing data into prompt and delayed events. We develop a new rigorous Bayesian analysis for the energy and timing data. We find that the data adds substantial statistical constraining power, and favors a BSM interpretation at the $\lesssim 2\sigma$ level.

The released data also provides an opportunity to search for light dark matter which couples with light mediators. The DM event under consideration is initiated by the production of a dark photon decaying into a pair of DM particles (e.g., Refs. [52, 53]). A DM particle would then induce a nuclear recoil event at the detector. The dark photon production can occur from both $\pi^-$ and $\pi^0$. Most of the $\pi^-$ are stopped inside

*Parts of this section are reprinted with permission from:

B. Dutta, S. Liao, S. Sinha, and L. E. Strigari, "Searching for Beyond the Standard Model Physics with COHERENT Energy and Timing Data," *Phys. Rev. Lett.* **123** no. 6, (2019) 061801, `arXiv: 1903.10666 [hep-ph]`. Published by the American Physical Society under the terms of the Creative Commons Attribution 4.0 International license

B. Dutta, D. Kim, S. Liao, J.-C. Park, S. Shin, and L. E. Strigari, "Dark matter signals from timing spectra at neutrino experiments," `arXiv: 1906.10745 [hep-ph]`. Submitted to Physical Review Letters

the Hg target and can create a dark photon via the absorption process, $\pi^- + p \to n + A'$, followed by the decay of the dark photon $A'$ to a DM pair [52]. The dark photon is emitted isotropically in this $\pi^-$ absorption process. The $\pi^0$ may produce an ordinary photon and a $A'$ [53]. We find that the DM flux reaching to the COHERENT detectors, which are located $\sim 90^\circ$ from the beam direction [38], is comparable to that from the $\pi^-$ absorption.

We develop a novel strategy that uses timing cut and energy cut on the data from COHERENT experiment to search for light DM. We find an excess in the timing and energy distribution which can be explained by DM as oppose to NSI of neutrinos.

### 5.1 Statistics framework for energy and timing analysis

To have a complete analysis of the two dimensional energy and timing data released from COHERENT, we first establish the statistics framework.

We define $\mathcal{L}$ as the likelihood function of the model parameters given the data. We assume that the sum of the observed nuclear recoil plus background counts, $N_{obs}(t, E)$, at time $t$ and energy $E$ follows a Poisson model with parameter

$$\lambda(t, E) = (1 + \alpha) N(t, E, \epsilon) + N_{bg}(t, E), \tag{5.1}$$

where $N(t, E, \epsilon)$ is the number of neutrino-induced nuclear recoil events predicted from the theory and $N_{bg}(t, E)$ denotes the true background count. Note that by definition $N_{bg}(t, E)$ is not observed. Rather, we have observed background counts, denoted by $N_{obs,bg}(t, E)$, that are proxy for the true background counts. We assume that given $N_{bg}(t, E)$, $N_{obs,bg}(t, E)$ follows a Poisson model with parameter $N_{bg}(t, E)$. In the absence of prior information on $N_{bg}(t, E)$, we use a non-informative prior on it, so that $\pi(N_{bg}(t, E)) \propto 1$ for $N_{bg}(t, E) \in [0, \infty)$.

In addition to the counts from the signal and the background components, Eq. (5.1) involves the uncertainty parameter $\alpha$ to account for the systematic uncertainties from

flux, form factor, quenching factor, and signal acceptance uncertainties. Motivated by the results reported from COHERENT [5], we assume this parameter follows a normal distribution with zero mean and standard deviation $\sigma_\alpha = 0.28$. Defining $\vec{\theta} = (g_e, g_\mu, m, R_n)$ as the model parameters, the most general likelihood function is

$$\mathcal{L}(\vec{\theta}|t,E) \propto \prod_{(t,E)} \int\int \exp\{-\lambda(t,E)\}\frac{\{\lambda(t,E)\}^{N_{obs}(t,E)}}{N_{obs}(t,E)!} \times \frac{\exp(-\alpha^2/2\sigma_\alpha^2)}{\sqrt{\sigma_\alpha^2}} \times \exp\{-N_{bg}(t,E)\}\frac{\{N_{bg}(t,E)\}^{N_{obs,bg}(t,E)}}{N_{obs,bg}(t,E)!}\,\mathrm{d}\alpha\,\mathrm{d}N_{bg}(t,E). \quad (5.2)$$

In comparison to previous analyses, this likelihood explicitly includes information from the timing distribution. We take the bin width in energy space as the bin width in the space of the number of photoelectrons, $n_e$, then convert this to recoil energy space using the relation $n_e = 1.17(E/\mathrm{keV})$. For the timing data we take the bin width directly from the COHERENT data, $\sim 0.5\mu$s. In the Bayesian paradigm we obtain the posterior probability densities for the model parameters using the multinest package [54] with flat prior distributions on the parameters.

For comparing two models, say models 0 and 1, where one is nested within another, we use the likelihood ratio test within a frequentist paradigm. We consider the test statistic $U = -2[\log(\mathcal{L}_0) - \log\{\mathcal{L}_1(\widehat{\theta})\}]$, where we define $\log(\mathcal{L}_0)$ as the log-likelihood for model 0 in which only $R_n$ is free and other three parameters are set to zero, and $\log\{\mathcal{L}_1(\widehat{\theta})\}$ is the log-likelihood for the model in which at least one of the parameters in $(g_e, g_\mu, M_{Z'})$ is free. For the latter model, $\widehat{\theta}$ denotes the maximum likelihood estimator (MLE) of $\vec{\theta}$, and $\widehat{\theta}$ is obtained by maximizing the marginal likelihood, Equation 5.2 where $N_{bg}(t,E)$ is integrated out. The $p$-value of the test is $p = \Pr(\chi^2_\eta > U_{\mathrm{obs}})$, where $U_{\mathrm{obs}}$ is the observed value of $U$ and $\chi^2_\eta$ is the chi-square distribution with $\eta$ degree of freedom. Here, $\eta$ is the difference between the number of estimated parameters in models 0 and 1. A small $p$-value provides significant evidence against the null hypothesis (SM). Applying this general procedure we can test if a model parameter

(i.e., $g_\mu$ or $g_e$) is positive. The corresponding significance $Z$ is $\Phi^{-1}(1-p/2)$, where $\Phi^{-1}$ is the inverse cumulative distribution function of the standard normal distribution. Significant results can also be seen through a large value of $Z$.

## 5.2 Timing and energy spectra of neutrino and dark matter in COHERENT experiment

COHERENT uses a proton beam on a Hg target at Spallation Neutron Source (SNS). Among the produced pions, $\pi^+$ first decays at rest to $\nu_\mu$ (prompt neutrino) and $\mu^+$; the $\mu^+$ decays in flight to $e^+$, $\nu_e$ and $\bar{\nu}_\mu$ (delayed neutrino). The energy spectra of neutrinos is therefore easily calculated with kinematics:

$$\begin{aligned} f_{\nu_\mu} &= \delta\left(E_\nu - \frac{m_\pi^2 - m_\mu^2}{2m_\pi}\right) \\ f_{\bar{\nu}_\mu} &= \frac{64}{m_\mu}\left[\left(\frac{E_\nu}{m_\mu}\right)^2\left(\frac{3}{4} - \frac{E_\nu}{m_\mu}\right)\right] \\ f_{\nu_e} &= \frac{192}{m_\mu}\left[\left(\frac{E_\nu}{m_\mu}\right)^2\left(\frac{1}{2} - \frac{E_\nu}{m_\mu}\right)\right] \end{aligned} \tag{5.3}$$

The timing spectra POT of SNS neutrino source has a peak at $0.7\mu s$ and width $0.15\mu s$ [14]. The timing spectra of prompt neutrino is therefore a convolution the POT with an exponential decay of $26ns$. The timing spectra of delayed neutrino is calculateb the convolution of the prompt neutrino with an exponential decay of $2.2\mu s$.

We show the theoretical calculation of neutrino energy and timing spectra of in Figure 5.1. This will be used in the analysis to compare with the observed nucleus recoil events in the data release.

To derive the energy and timing spectra of dark matter in COHERENT experiment, we consider the following Lagrangian:

$$\mathcal{L}_{\text{int}} \supset g_\chi A'_\mu \bar{\chi}\gamma^\mu\chi + e_q\epsilon_1^q A'_\mu \bar{q}\gamma^\mu q\,, \tag{5.4}$$

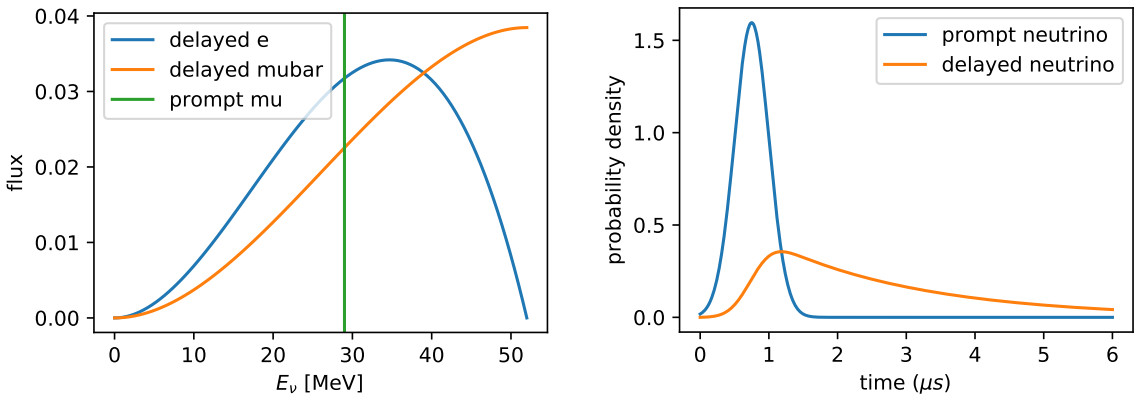


Figure 5.1: Energy and timing spectra at COHERENT experiment.

where $e_q = eQ_q$ and where $g_\chi$ and $\epsilon_1^q$ are dark-sector gauge coupling and kinetic mixing parameter (associated with the mixing between the photon and new gauge Boson $\frac{\epsilon}{2}F^{\mu\nu\prime}F_{\mu\nu}$ [55–57]), respectively. This generic-looking Lagrangian can be accommodated in the context of a model in e.g., [52, 58].

The $\pi^-$ and $\pi^0$ produced in the proton beam hitting on target decay into dark photon $A'$ and then the dark photon decays into dark matter which induces nucleus recoil. We use numerical simulation to track the energy and timing information of each dark matter particle. The relevant code is published as an open source python package, and can be accessed at GitHub (https://github.com/Ikaroshu/pyCEvNS). In Figure 5.2, we show the timing distribution of dark matter as well as the recoil spectrum. We can see that (by comparing to Figure 5.1) a time cut around $1.5\mu s$ and energy cut around 14keV will factor out most of neutrino background in search of dark matter signals. Regarding DM-nucleus scattering, we remark that in principle DM scattering can be governed by physics different from that for dark photon production encoded in Eq. (5.4). Introducing a generic mediator of mass $M'$, DM-mediator coupling $g_D$, and quark-mediator coupling $e\epsilon_q$, we find that the differential spectrum in recoil energy $E_r$

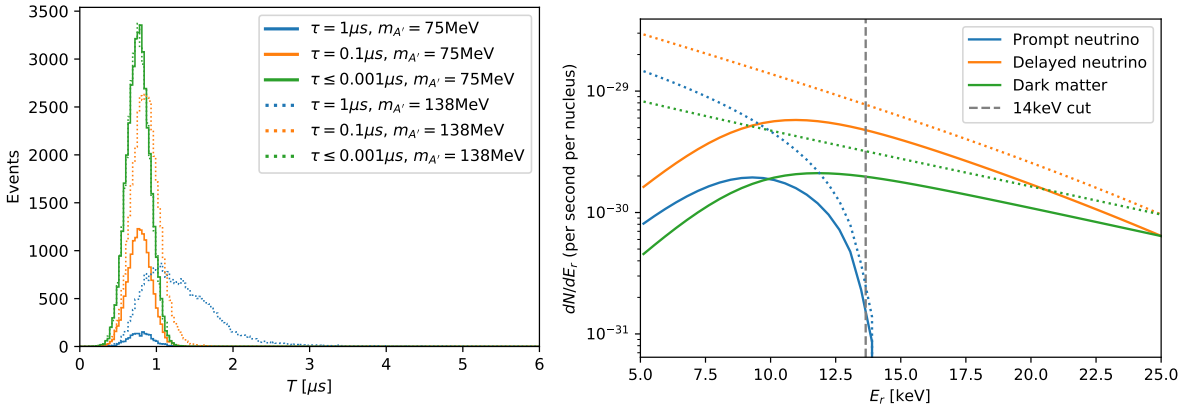


Figure 5.2: Left: Timing spectra of DM signal with three different values for $\tau_{A'}$, in a relativistic $A'$ scenario (solid) and a non-relativistic $A'$ scenario (dashed). Right: Nuclear recoil spectrum produced from neutrino and DM interactions with (solid) and without (dashed) experimental efficiencies. The vertical dashed line indicates the energy cut that is used to eliminate prompt $\nu$-induced events. Reprinted with permission from [1].

of the target nucleus can be expressed as

$$\frac{d\sigma}{dE_r} = \frac{e^2(\epsilon_2^q)^2 g_D^2 Z^2 \cdot |F(2m_N E_r)|^2}{4\pi p_\chi^2 (2m_N E_r + M'^2)^2} \left\{ 2E_\chi^2 m_N \left(1 - \frac{E_r}{E_\chi} - \frac{m_N E_r}{2E_\chi^2}\right) + E_r^2 m_N \right\} \quad (5.5)$$

where $F$ denotes the form factor and where $Z$ and $m_N$ are the atomic number and the mass of the target nucleus. The underlying interaction is of dark-photon type for illustration. We neglected $m_\chi$ in the curly brackets as $m_N \gg m_\chi$. Clearly, the spectral behavior is (nearly) independent of $m_\chi$.

## 5.3 Results and analysis

Equipped with the theoretical calculation of neutrino and dark matter spectra in energy and time dimension. We are now ready to constrain BSM using COHERENT data release.

### 5.3.1 *Constraining NSI of neutrino with full COHERENT energy and timing data*

In order to simplify our analysis, for our BSM scenario we consider models with couplings such that $g_\nu = g_u = g_d = g'$. To compare the sensitivity of the data to different flavors, we either fit for $g_\mu$ and fix $g_e$, or vice versa. The key features of our analysis are unchanged if we use a different relation among the couplings.

First we fix the mediator mass at 10MeV and 1000MeV to show energy plus timing give may imply BSM. In Figure 5.3, we show the resulting posterior probability distributions for $g_\mu$ (assuming that $g_e = 0$), for the cases of $M_{Z'} = 10$ and 1000 MeV. The figures contain distributions using energy information alone, and distributions using both energy and timing information. For both $M_{Z'} = 10$ and 1000 MeV, the $g_\mu$ distributions are better constrained when including timing data, and deviate from the SM prediction that these couplings are zero. We also consider the case with form factor (detail discussion in previous chapter). We apply likelihood ratio test to the result and find the significance $Z = 1.6$ for both mediator masses. On the other hand, we get $Z = 1$ without timing information. This implies that the timing data provides additional information on the flavor content of the fluxes that is not provided by the energy data alone. The bin-by-bin likelihood analysis that we employ is able to statistically separate the prompt and delayed distributions, with the timing information more strongly constraining the prompt $g_\mu$ component. In contrast, the $g_e$ component only contributes to delayed neutrino recoil spectrum, and is less well constrained when adding in the timing information.

Next, we consider the constraints on full $g$ v.s. $M_{Z'}$ parameter space. Figure 5.4 shows the probability density in $\log_{10}(M_{Z'})$ vs $\log_{10}(g_\mu)$ or $\log_{10}(g_\mu/\Lambda)$ space. The shape of the boundary in both plots can be understood as follows: in the small mediator mass region, $q^2 \gg M_{Z'}^2$, the NSI parameter is independent of the small mediator mass, while in the large mediator mass region, $M_{Z'}^2 \gg q^2$, the NSI parameter depends on $g^2/M_{Z'}^2$, thus, in log space the slope is about 1. The isolated island at large mediator

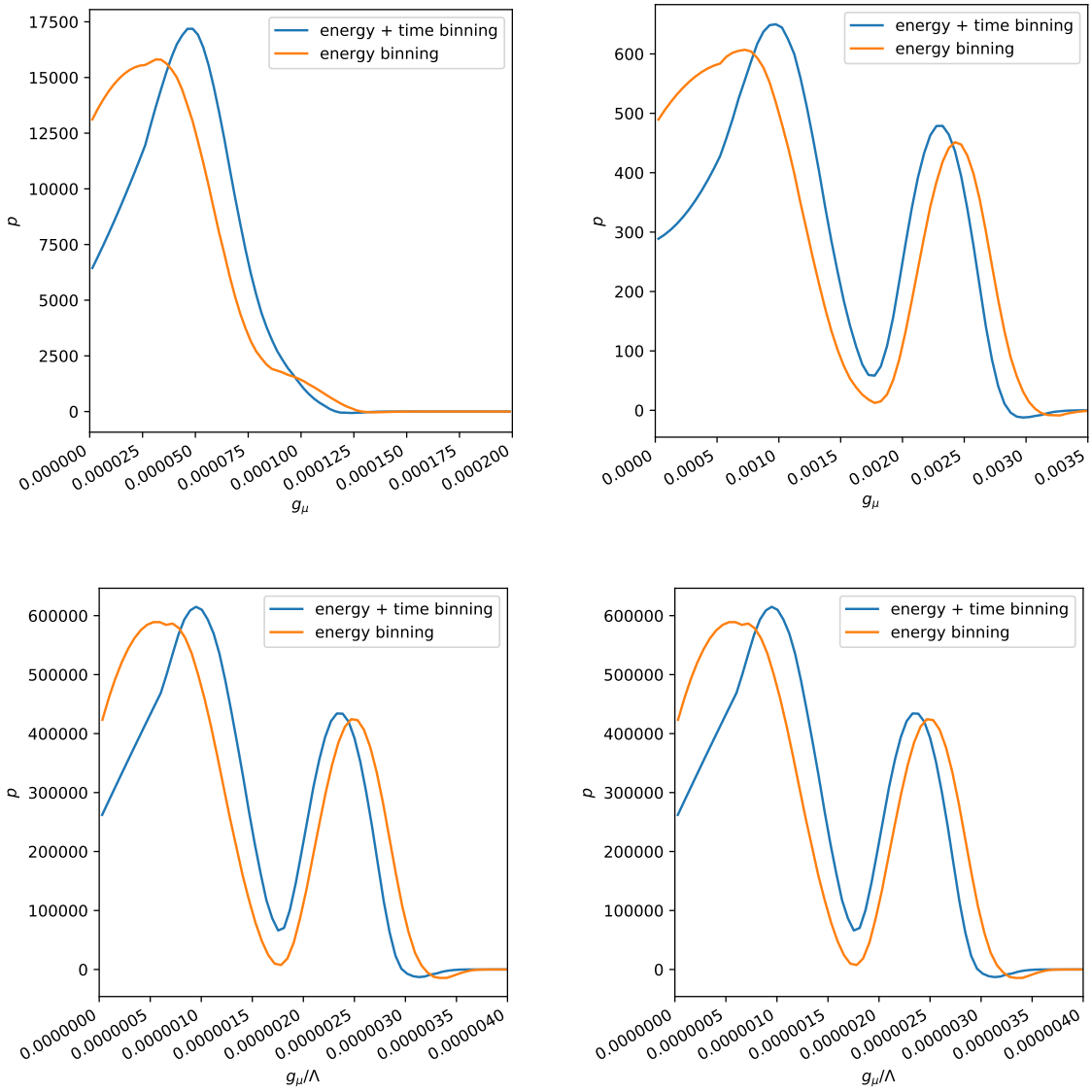


Figure 5.3: Posterior probability distributions for $g_\mu$ (top row) or $g_\mu/\Lambda$ (bottom row, if there is form factor), using the energy data alone (orange) and using the combined energy and timing data (blue). The left column assumes a mediator mass of $M_{Z'} = 10$ MeV, and the right column assumes a mediator mass of $M_{Z'} = 1000$ MeV. Reprinted with permission from [15].

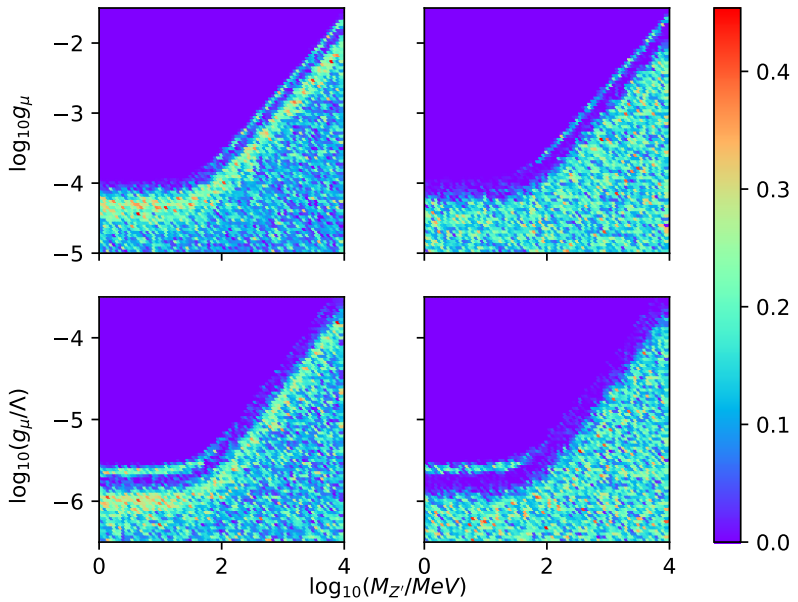


Figure 5.4: Heat map of the probability density in $\log_{10}(M_{Z'})$ vs $\log_{10} g_\mu$ (top row) and $\log_{10}(M_{Z'})$ vs $\log_{10}(g_\mu/\Lambda)$ (bottom row, for a form factor $q^2/\Lambda^2$) parameter space using energy and timing data (left) and energy data alone (right). Reprinted with permission from [15].

mass region is because the global degeneracy for the weak charge across all energy bins (since the NSI parameter is independent of energy), thus, the constraint on the charge $Q_v$ in Equation 2.22 results in two solutions for $g$. On the contrary, if a hidden sector is introduced to generate a form factor $\sim q^2/\Lambda^2$, the NSI parameter becomes independent of energy in the smaller mass region and consequently, the degeneracy appears in the smaller mass region.

To quantify the constraints on the NSI parameters in Figure 5.4, we show in Table 5.1 the $1\sigma$ window of $g_\mu$ and $g_e$ assuming 10, 100, and 1000 MeV mediator masses using our results from the energy and timing analysis. Note that this range is consistent with general constraints on the couplings and masses of light mediators [59].

| $M_{Z'}$ (MeV) | 10 | 100 | 1000 |
|---|---|---|---|
| $g_\mu$ | $[1.87, 6.65] \times 10^{-5}$ | $[0.41, 1.47] \times 10^{-4} \oplus [2.47, 2.66] \times 10^{-4}$ | $[0.48, 1.32] \times 10^{-3} \oplus [2.17, 2.47] \times 10^{-3}$ |
| $g_e$ | $[0, 6.12] \times 10^{-5}$ | $[0, 1.53] \times 10^{-4} \oplus [2.53, 2.84] \times 10^{-4}$ | $[0, 1.22] \times 10^{-3} \oplus [2.22, 2.77] \times 10^{-3}$ |

Table 5.1: The $1\sigma$ constraining range on $g_\mu$ and $g_e$ using energy plus timing information. Reprinted with permission from [15].

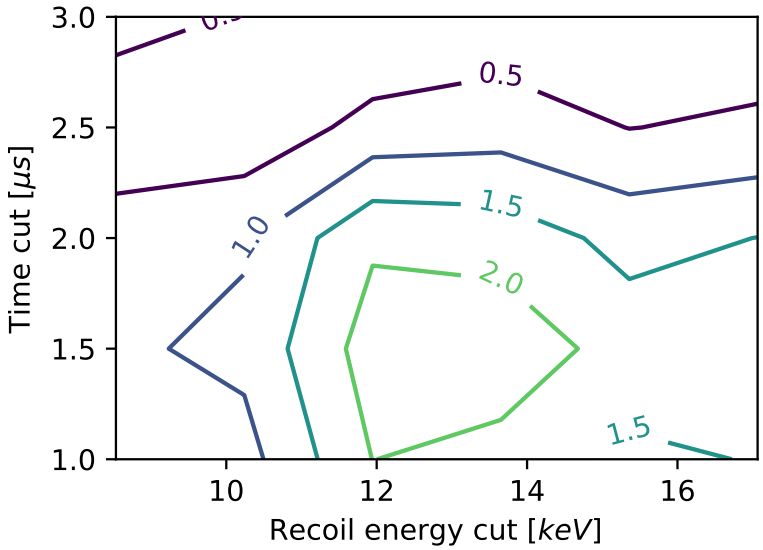


Figure 5.5: The significance contour with various cut on energy and timing dimension on COHERENT data.

### *5.3.2 DM signal with energy and timing cut*

First we can optimize our energy and timing cut by scanning through the data. In Figure 5.5, we show the contour of significances with various cut in the energy and timing space. We find the cut is optimized with $E_r > 14$ keV (16 photoelectrons) and $T < 1.5$ $\mu$s to substantially suppress both prompt and delayed neutrino events. After these cuts, we find 97 total events. Out of them 49 events have been classified as the steady-state (SS) background, while 19 may be identified as delayed neutrino events forming the SM (i.e., neutrino) background. There are also 3 events in the cut window arising from beam related neutron (BRN) backgrounds. There is then an "excess"

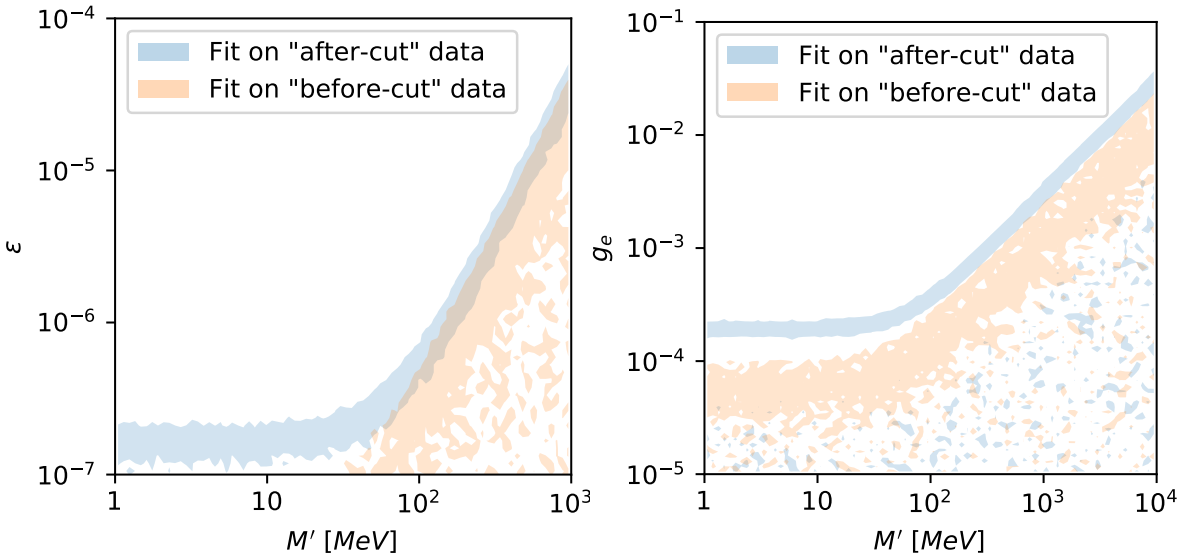


Figure 5.6: $1\sigma$ best fits to the "before-cut" data (orange) and the "after-cut" data (blue) for a DM interpretation (left panel) and a neutrino NSI interpretation (right panel). Reprinted with permission from [1].

of 26 events which corresponds to a $2.4\sigma$ statistical uncertainty. For calculating the significance we apply Excess $= (\text{signal} - \text{SS} - \text{BRN} - \text{SM})/\sqrt{2\,\text{SS} + \text{BRN} + \text{SM}}$ [5].

The excess can be explained by DM interpretation as well as neutrino interpretation. In Figure 5.6 we compare the two interpretation of the fit to the data before or after applying the cuts. For the DM interpretation, we see that there exists an overlapping region, and further find that both "before-cut" and "after-cut" data sets are well accommodated by the parameter points with $M' \gtrsim 100$ MeV. As a comparison, the NSI neutrino hypothesis is not able to fit the "before-cut" and "after-cut" data simultaneously.

In the DM scenario, the mediator may not necessarily be dark photons in Equation 5.4. The above $\epsilon$ is the effective coupling defined as $\epsilon = \epsilon_1^q \epsilon_2^q \epsilon_D \sqrt{\text{BR}_{A' \to \chi\chi}}$, where $\epsilon_1^q$ is the $q$-$A'$ kinetic mixing which describes the dark photon production from the $\pi^-$ absorption, $\epsilon_2^q$ is the quark-mediator kinetic mixing for the DM-nucleus scattering cross-section, and $g_D = e\epsilon_D$ is the DM-mediator coupling. In Table 5.2, we summarize the best fit of $\epsilon^q$ in the case of single mediator scenario where dark photon acts as

| $M'$ | 50 | 75 | 100 | 1000 |
|---|---|---|---|---|
| $\epsilon^q$ | $3.5 \times 10^{-4}$ | $4.4 \times 10^{-4}$ | $5.5 \times 10^{-4}$ | $4.6 \times 10^{-3}$ |

Table 5.2: Best-fit $\epsilon^q$ for a few $M'$ values (in MeV) for the single-mediator scenario. Reprinted with permission from [1].

mediator. In this case, $\epsilon = \epsilon_1^q \epsilon_2^q \epsilon_D \sqrt{\text{BR}_{A' \to \chi\chi}} \to (\epsilon^q)^2 \epsilon_D \sqrt{\text{BR}_{A' \to \chi\chi}}$. We can choose $\epsilon_D = 1/e$ to make $g_D = 1$ which makes $\tau_{A'}$ small, and we can still make use of the left panel of Figure 5.6 (where $\tau_{A'}$ is set to be $\leq 1$ ns). With dark photon differs from mediator, Table 5.2 still holds with $\epsilon^q$ identified as $\sqrt{\epsilon_1^q \epsilon_2^q \epsilon_D e}$.

Using the same strategy, we can project the limits of future COHERENT experiments with larger exposure. We compare the current and future limits with LDMX and NA64 results in Figure 5.7. We find the limits complements both LDMX and NA64 results at large mediator mass [60, 61]. In the plot, there are two scenarios: (i) the dark photon coupling ($\epsilon_1^q$) is the same as the mediator-nucleus coupling ($\epsilon_2^q$) and (ii) $\epsilon_1^q$ is fixed at $10^{-2}$ (current experimental constraint [62]) with $\alpha_D \equiv g_D^2/(4\pi) = 0.5$. We use a dark photon mass $m_{A'} = 75$ MeV and a DM mass $m_\chi = 5$ MeV. The figure, however, is unchanged for $m_{A'} \leq 138$ MeV, $m_\chi \leq m_{A'}/2$ and $\tau_{A'} \leq 4$ ns.

## 5.4 Conclusion

In this chapter, we have analyzed the COHERENT data release. The extra timing information enables the ability of probing flavor of neutrinos which is impossible in the CE$\nu$NS experiments using energy alone. We have derived the general statistics framework for the analysis including both energy and timing. We have discovered that there is a $\sim 2\sigma$ deviation between the best-fitting model and the SM prediction.

With a combination of timing and energy cut, we have shown it eliminates the SM neutrino events effectively. As applied to published data, we have discovered that the DM interpretation of the excess fits the after-cut data as well as before-cut data. On the other hand, neutrino NSI fails to fit the full and cut data at the same time. This

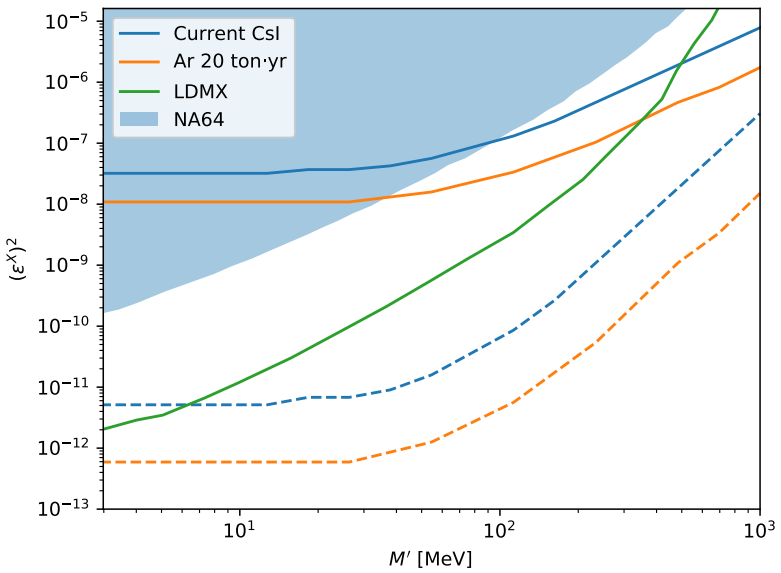


Figure 5.7: The coupling $(\epsilon^X)^2$ for mediator-nucleus coupling is shown as a function of $M'$. The solid (dashed) lines assume $\epsilon^X = \epsilon^q_1 = \epsilon^q_2$ ($\epsilon^X = \epsilon^q_{1,2}$ with $\epsilon^q_{2,1} = 10^{-2}$). $\epsilon^X$ for LDMX can be understood as $\epsilon$ in Ref. [60]. Reprinted with permission from [1].

contradicts our previous discovery. However, it is worth noting that it remains possible the excess may be explained by an unidentified background or systematic uncertainty. Nevertheless, our proposed strategy is able to complement existing dark matter search experiment and can be generalized to other experiments similar to COHERENT setup.

# 6. CONCLUSION

The rich phenomenology of neutrino scattering off nucleus and electron provides an ideal source of probing beyond Standard Model. The experiments on the scattering of neutrinos help the understanding of not only neutrino physics itself, but also dark matters. This work explored various aspect of BSM physics that neutrino scattering experiments can probe.

We began our analysis with ultra-low threshold detector in neutrino scattering experiment. After defining the general neutral current interaction of neutrinos, we gave the discovery limits on the scalar, pseudo-scalar, vector, and axial-vector couplings of NSI. The vector coupling is particular interesting, as it is related to many of the BSM models and also appears in the neutrino oscillation experiments. However, the degeneracies between the flavors of the neutrino NSI couplings makes it impossible to constrain the parameters space well enough with a single experiment. We therefore proposed that the with multi-detector and multi-source of neutrino scattering experiment, it is possible to break the degeneracies. The breaking of degeneracies also help complement the neutrino oscillation experiments which otherwise cannot distinguish the up or down quark contribution of the NSI parameters.

With the general NSI of neutrino defined, we inspected models falls in the realm of NSI. Specifically, we discussed kinetic and mass mixing effects as well as a $q^2$ form factor induced by a loop of hidden sector. We found that neutrino scattering experiments are able to put new constraints on top of existing experiment results.

Future dark matter direct detection experiments can also serve as neutrino experiments. Understanding the neutrino behavior not only helps neutrino physics but also help distinguish dark matter signals from neutrino signals in dark matter experiments. We analyzed the effects of solar neutrinos in dark matter direct detection experiments in the presence of NSI. We include the NSI of neutrino in both oscillation and detec-

tion of neutrinos, and found that the matter effects can play important roles of in the detection of solar neutrinos in the dark matter experiments. The LMA-D solution of neutrino oscillation experiments can therefore be resolved.

Finally, we analyzed the recently released COHERENT experiment data with energy and timing information. In order to enable the analysis of this two dimensional data with not-well-understood steady state background, we developed a likelihood analysis in Bayesian framework. We found the full energy and timing analysis favors BSM over SM in terms non-standard interactions of neutrino. However, with energy and timing cut optimized, we found there is an excessive events after removing most of the neutrino signals. The excess cannot be explained by the NSI interpretation, instead, we found DM interpretation fits both before-cut and after-cut data. The same optimization strategy can be applied to future COHERENT-like experiments, and has projected limits that complements existing dark matter experiments.

REFERENCES


[1] B. Dutta, D. Kim, S. Liao, J.-C. Park, S. Shin, and L. E. Strigari, "Dark matter signals from timing spectra at neutrino experiments," arXiv:1906.10745 [hep-ph].

[2] J. B. Dent, B. Dutta, D. Kim, S. Liao, R. Mahapatra, K. Sinha, and A. Thompson, "New Directions for Axion Searches via Scattering at Reactor Neutrino Experiments," arXiv:1912.05733 [hep-ph].

[3] D. Z. Freedman, "Coherent Neutrino Nucleus Scattering as a Probe of the Weak Neutral Current," *Phys. Rev.* **D9** (1974) 1389–1392.

[4] D. Baxter *et al.*, "Coherent Elastic Neutrino-Nucleus Scattering at the European Spallation Source," arXiv:1911.00762 [physics.ins-det].

[5] **COHERENT** Collaboration, D. Akimov *et al.*, "Observation of Coherent Elastic Neutrino-Nucleus Scattering," *Science* **357** no. 6356, (2017) 1123–1126, arXiv:1708.01294 [nucl-ex].

[6] **MINER** Collaboration, G. Agnolet *et al.*, "Background Studies for the MINER Coherent Neutrino Scattering Reactor Experiment," *Nucl. Instrum. Meth.* **A853** (2017) 53–60, arXiv:1609.02066 [physics.ins-det].

[7] J. B. Dent, B. Dutta, S. Liao, J. L. Newstead, L. E. Strigari, and J. W. Walker, "Probing light mediators at ultralow threshold energies with coherent elastic neutrino-nucleus scattering," *Phys. Rev.* **D96** no. 9, (2017) 095007, arXiv:1612.06350 [hep-ph].

[8] J. B. Dent, B. Dutta, S. Liao, J. L. Newstead, L. E. Strigari, and J. W. Walker, "Accelerator and reactor complementarity in coherent neutrino-nucleus scattering," *Phys. Rev.* **D97** no. 3, (2018) 035009, arXiv:1711.03521 [hep-ph].

[9] M. Abdullah, J. B. Dent, B. Dutta, G. L. Kane, S. Liao, and L. E. Strigari, "Coherent elastic neutrino nucleus scattering as a probe of a Z through kinetic

and mass mixing effects," *Phys. Rev.* **D98** no. 1, (2018) 015005, arXiv:1803.01224 [hep-ph].

[10] A. Datta, B. Dutta, S. Liao, D. Marfatia, and L. E. Strigari, "Neutrino scattering and B anomalies from hidden sector portals," *JHEP* **01** (2019) 091, arXiv:1808.02611 [hep-ph].

[11] J. Monroe and P. Fisher, "Neutrino Backgrounds to Dark Matter Searches," *Phys. Rev.* **D76** (2007) 033007, arXiv:0706.3019 [astro-ph].

[12] **XENON** Collaboration, E. Aprile *et al.*, "Physics reach of the XENON1T dark matter experiment," *JCAP* **1604** no. 04, (2016) 027, arXiv:1512.07501 [physics.ins-det].

[13] B. Dutta, S. Liao, L. E. Strigari, and J. W. Walker, "Non-standard interactions of solar neutrinos in dark matter experiments," *Phys. Lett.* **B773** (2017) 242–246, arXiv:1705.00661 [hep-ph].

[14] **COHERENT** Collaboration, D. Akimov *et al.*, "COHERENT Collaboration data release from the first observation of coherent elastic neutrino-nucleus scattering," arXiv:1804.09459 [nucl-ex].

[15] B. Dutta, S. Liao, S. Sinha, and L. E. Strigari, "Searching for Beyond the Standard Model Physics with COHERENT Energy and Timing Data," *Phys. Rev. Lett.* **123** no. 6, (2019) 061801, arXiv:1903.10666 [hep-ph].

[16] R. H. Helm, "Inelastic and Elastic Scattering of 187-Mev Electrons from Selected Even-Even Nuclei," *Phys. Rev.* **104** (1956) 1466–1475.

[17] **XENON100** Collaboration, E. Aprile *et al.*, "Limits on spin-dependent WIMP-nucleon cross sections from 225 live days of XENON100 data," *Phys. Rev. Lett.* **111** no. 2, (2013) 021301, arXiv:1301.6620 [astro-ph.CO].

[18] A. Crivellin, M. Hoferichter, and M. Procura, "Accurate evaluation of hadronic uncertainties in spin-independent WIMP-nucleon scattering: Disentangling two- and three-flavor effects," *Phys. Rev.* **D89** (2014) 054021, arXiv:1312.4951

[hep-ph].

[19] M. Hoferichter, J. Ruiz de Elvira, B. Kubis, and U.-G. MeiSSner, "High-Precision Determination of the Pion-Nucleon Term from Roy-Steiner Equations," *Phys. Rev. Lett.* **115** (2015) 092301, arXiv:1506.04142 [hep-ph].

[20] Y. Farzan and M. Tortola, "Neutrino oscillations and Non-Standard Interactions," *Front.in Phys.* **6** (2018) 10, arXiv:1710.09360 [hep-ph].

[21] O. G. Miranda and H. Nunokawa, "Non standard neutrino interactions: current status and future prospects," *New J. Phys.* **17** no. 9, (2015) 095002, arXiv:1505.06254 [hep-ph].

[22] T. Ohlsson, "Status of non-standard neutrino interactions," *Rept. Prog. Phys.* **76** (2013) 044201, arXiv:1209.2710 [hep-ph].

[23] W. Haxton, R. Hamish Robertson, and A. M. Serenelli, "Solar neutrinos: Status and prospects," *Ann.Rev.Astron.Astrophys.* **51** (2013) 21–61, arXiv:1208.5723 [astro-ph.SR].

[24] G. Cowan, K. Cranmer, E. Gross, and O. Vitells, "Asymptotic formulae for likelihood-based tests of new physics," *Eur. Phys. J.* **C71** (2011) 1554, arXiv:1007.1727 [physics.data-an]. [Erratum: Eur. Phys. J.C73,2501(2013)].

[25] P. Langacker, "Grand Unified Theories and Proton Decay," *Phys. Rept.* **72** (1981) 185.

[26] A. E. Faraggi and D. V. Nanopoulos, "A SUPERSTRING $Z'$ AT O (1-TeV) ?," *Mod. Phys. Lett.* **A6** (1991) 61–68.

[27] R. Gauld, F. Goertz, and U. Haisch, "An explicit Z'-boson explanation of the $B \to K^* \mu^+ \mu^-$ anomaly," *JHEP* **01** (2014) 069, arXiv:1310.1082 [hep-ph].

[28] H. Davoudiasl, H.-S. Lee, and W. J. Marciano, "'Dark' Z implications for Parity Violation, Rare Meson Decays, and Higgs Physics," *Phys. Rev.* **D85** (2012) 115019, arXiv:1203.2947 [hep-ph].

[29] X.-G. He, G. C. Joshi, H. Lew, and R. R. Volkas, "Simplest Z-prime model," *Phys. Rev.* **D44** (1991) 2118–2132.

[30] X. G. He, G. C. Joshi, H. Lew, and R. R. Volkas, "NEW Z-prime PHENOMENOLOGY," *Phys. Rev.* **D43** (1991) 22–24.

[31] J. Heeck, M. Holthausen, W. Rodejohann, and Y. Shimizu, "Higgs ??? in Abelian and non-Abelian flavor symmetry models," *Nucl. Phys.* **B896** (2015) 281–310, arXiv:1412.3671 [hep-ph].

[32] W. Altmannshofer, S. Gori, S. Profumo, and F. S. Queiroz, "Explaining dark matter and B decay anomalies with an $L_\mu - L_\tau$ model," *JHEP* **12** (2016) 106, arXiv:1609.04026 [hep-ph].

[33] A. Datta, J. Kumar, J. Liao, and D. Marfatia, "New light mediators for the $R_K$ and $R_{K^*}$ puzzles," *Phys. Rev.* **D97** no. 11, (2018) 115038, arXiv:1705.08423 [hep-ph].

[34] A. Datta, M. Duraisamy, and D. Ghosh, "Explaining the $B \to K^* \mu^+ \mu^-$ data with scalar interactions," *Phys. Rev.* **D89** no. 7, (2014) 071501, arXiv:1310.1937 [hep-ph].

[35] **CONNIE** Collaboration, A. Aguilar-Arevalo *et al.*, "The CONNIE experiment," *J. Phys. Conf. Ser.* **761** no. 1, (2016) 012057, arXiv:1608.01565 [physics.ins-det].

[36] **TEXONO** Collaboration, H. Bin Li, "Neutrino and dark matter physics with sub-KeV Germanium detectors," *J. Phys. Conf. Ser.* **718** no. 6, (2016) 062036.

[37] **MINER** Collaboration, G. Agnolet *et al.*, "Background Studies for the MINER Coherent Neutrino Scattering Reactor Experiment," *Nucl. Instrum. Meth.* **A853** (2017) 53–60, arXiv:1609.02066 [physics.ins-det].

[38] **COHERENT** Collaboration, D. Akimov *et al.*, "COHERENT 2018 at the Spallation Neutron Source," arXiv:1803.09183 [physics.ins-det].

[39] **Daya Bay** Collaboration, F. P. An *et al.*, "Improved Measurement of the

Reactor Antineutrino Flux and Spectrum at Daya Bay," *Chin. Phys.* **C41** no. 1, (2017) 013002, arXiv:1607.05378 [hep-ex].

[40] B. S. Acharya, S. A. R. Ellis, G. L. Kane, B. D. Nelson, and M. J. Perry, "The lightest visible-sector supersymmetric particle is likely to be unstable," *Phys. Rev. Lett.* **117** (2016) 181802, arXiv:1604.05320 [hep-ph].

[41] **Borexino** Collaboration, M. Agostini *et al.*, "First simultaneous precision spectroscopy of *pp*, $^{7}$be, and *pep* solar neutrinos with borexino phase-ii," *Phys.Rev.D* **100** no. 8, (2019) 082004, arXiv:1707.09279 [hep-ex].

[42] J. Billard, L. Strigari, and E. Figueroa-Feliciano, "Implication of neutrino backgrounds on the reach of next generation dark matter direct detection experiments," *Phys. Rev.* **D89** no. 2, (2014) 023524, arXiv:1307.5458 [hep-ph].

[43] B. Mount *et al.*, "Lux-zeplin (lz) technical design report," tech. rep. arXiv:1703.09144 [physics.ins-det].

[44] T.-K. Kuo and J. T. Pantaleone, "Neutrino oscillations in matter," *Rev.Mod.Phys.* **61** (1989) 937.

[45] A. Friedland, C. Lunardini, and C. Pena-Garay, "Solar neutrinos as probes of neutrino matter interactions," *Phys.Lett.B* **594** (2004) 347, arXiv:hep-ph/0402266.

[46] **Particle Data Group** Collaboration, C. Patrignani *et al.*, "Review of particle physics," *Chin.Phys.C* **40** no. 10, (2016) 100001.

[47] V. Antonelli, L. Miramonti, C. Pena Garay, and A. Serenelli, "Solar neutrinos," *Adv.High Energy Phys.* **2013** (2013) 351926, arXiv:1208.1356 [hep-ex].

[48] **LZ** Collaboration, D. Akerib *et al.*, "Lux-zeplin (lz) conceptual design report," tech. rep. arXiv:1509.02910 [physics.ins-det].

[49] M. Gonzalez-Garcia and M. Maltoni, "Determination of matter potential from global analysis of neutrino oscillation data," *JHEP* **09** (2013) 152,

arXiv:1307.3092 [hep-ph].

[50] O. Miranda, M. Tortola, and J. Valle, "Are solar neutrino oscillations robust?" *JHEP* **10** (2006) 008, arXiv:hep-ph/0406280.

[51] P. B. Denton, Y. Farzan, and I. M. Shoemaker, "Testing large non-standard neutrino interactions with arbitrary mediator mass after COHERENT data," *JHEP* **07** (2018) 037, arXiv:1804.03660 [hep-ph].

[52] P. deNiverville, M. Pospelov, and A. Ritz, "Light new physics in coherent neutrino-nucleus scattering experiments," *Phys. Rev.* **D92** no. 9, (2015) 095005, arXiv:1505.07805 [hep-ph].

[53] S.-F. Ge and I. M. Shoemaker, "Constraining Photon Portal Dark Matter with Texono and Coherent Data," *JHEP* **11** (2018) 066, arXiv:1710.10889 [hep-ph].

[54] F. Feroz, M. P. Hobson, and M. Bridges, "MultiNest: an efficient and robust Bayesian inference tool for cosmology and particle physics," *Mon. Not. Roy. Astron. Soc.* **398** (2009) 1601–1614, arXiv:0809.3437 [astro-ph].

[55] B. Holdom, "Two U(1)'s and Epsilon Charge Shifts," *Phys. Lett.* **166B** (1986) 196–198.

[56] F. del Aguila, G. D. Coughlan, and M. Quiros, "Gauge Coupling Renormalization With Several U(1) Factors," *Nucl. Phys.* **B307** (1988) 633. [Erratum: Nucl. Phys.B312,751(1989)].

[57] K. S. Babu, C. F. Kolda, and J. March-Russell, "Implications of generalized Z - Z-prime mixing," *Phys. Rev.* **D57** (1998) 6788–6792, arXiv:hep-ph/9710441 [hep-ph].

[58] B. Dutta, S. Ghosh, and J. Kumar, "A sub-GeV dark matter model," *Phys. Rev.* **D100** (2019) 075028, arXiv:1905.02692 [hep-ph].

[59] M. Bauer, P. Foldenauer, and J. Jaeckel, "Hunting All the Hidden Photons," *JHEP* **07** (2018) 094, arXiv:1803.05466 [hep-ph].

[60] **LDMX** Collaboration, T. Åkesson *et al.*, "Light Dark Matter eXperiment (LDMX)," arXiv:1808.05219 [hep-ex].

[61] D. Banerjee *et al.*, "Dark matter search in missing energy events with NA64," *Phys. Rev. Lett.* **123** no. 12, (2019) 121801, arXiv:1906.00176 [hep-ex].

[62] **BNL-E949** Collaboration, A. V. Artamonov *et al.*, "Study of the decay $K^+ \to \pi^+ \nu\bar{\nu}$ in the momentum region $140 < P_\pi < 199$ MeV/c," *Phys. Rev.* **D79** (2009) 092004, arXiv:0903.0030 [hep-ex].